nature chemistry

Supplementary information

https://doi.org/10.1038/s41557-026-02070-4

Homochiral toroidal spin state in Dy(III)-based single-molecule toroics

In the format provided by the authors and unedited

Contents

1. Synthesis and characterization

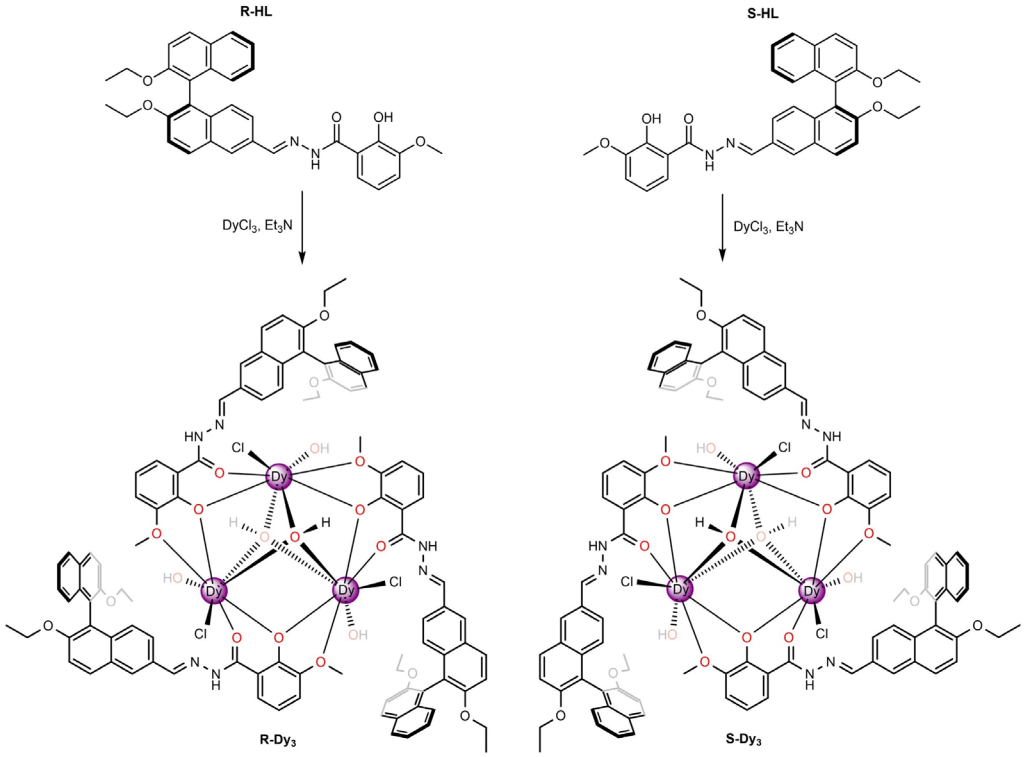

Supplementary Scheme 1 Synthetic route of **R/S-Dy3**.

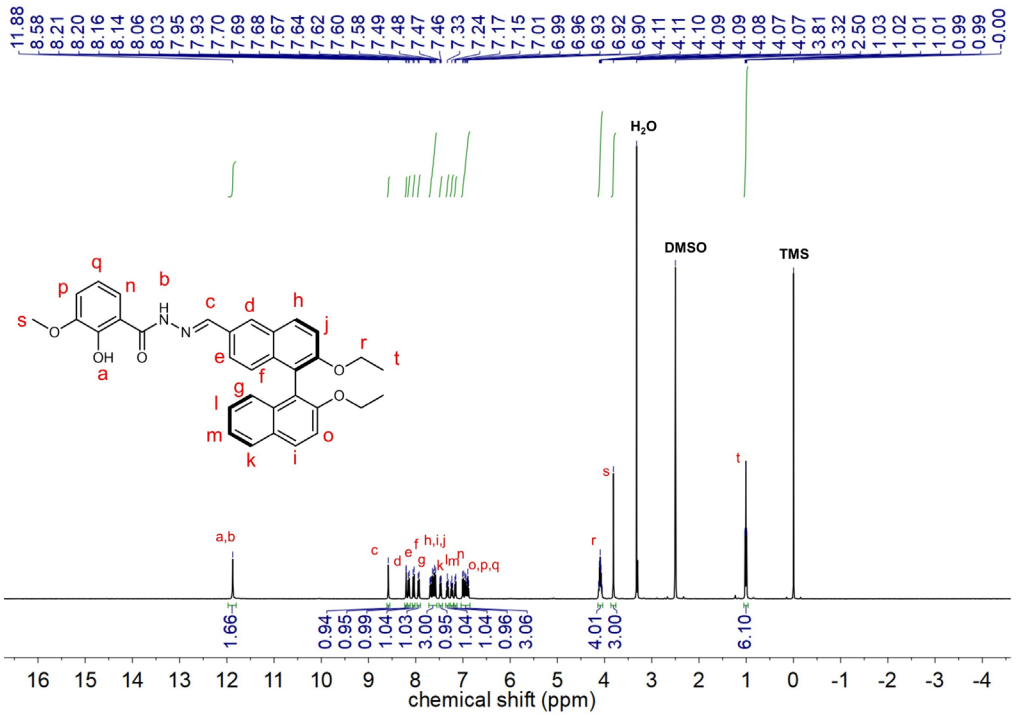

Supplementary Figure 1 ^{1}H NMR spectrum (400 MHz, $(CD_3)_2SO$) for **R-HL**.

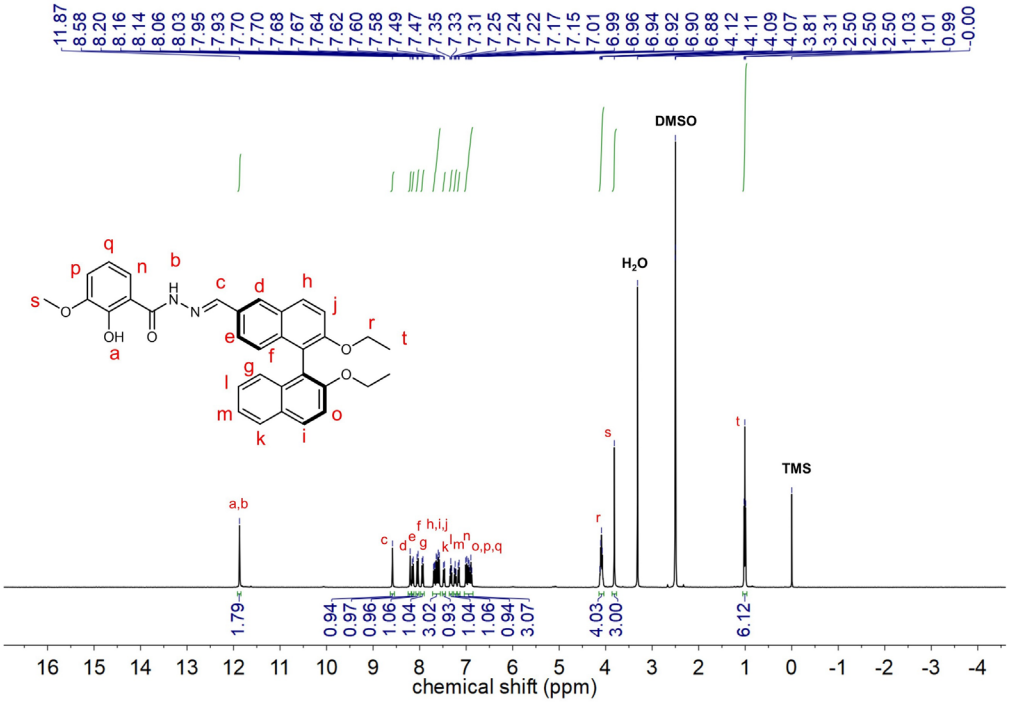

Supplementary Figure 2 ^{1}H NMR spectra (400 MHz, $(CD_3)_2SO$) for **S-HL**.

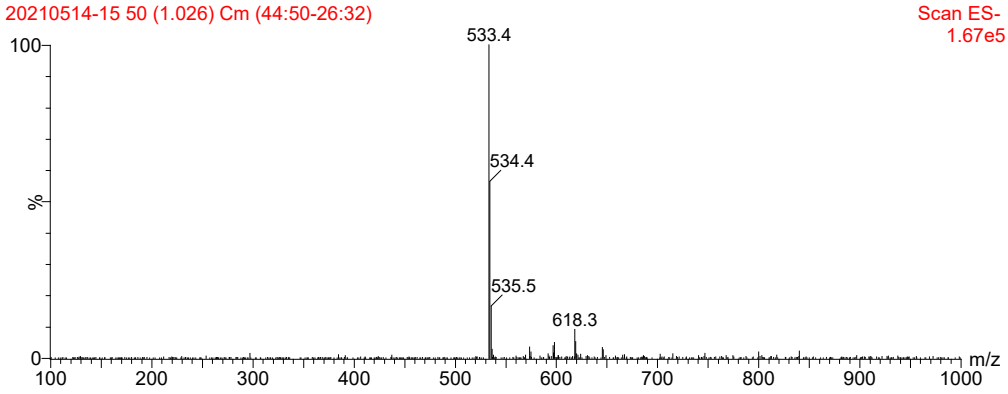

Supplementary Figure 3 ESI-MS spectrum for **R-HL** in CH_2Cl_2.

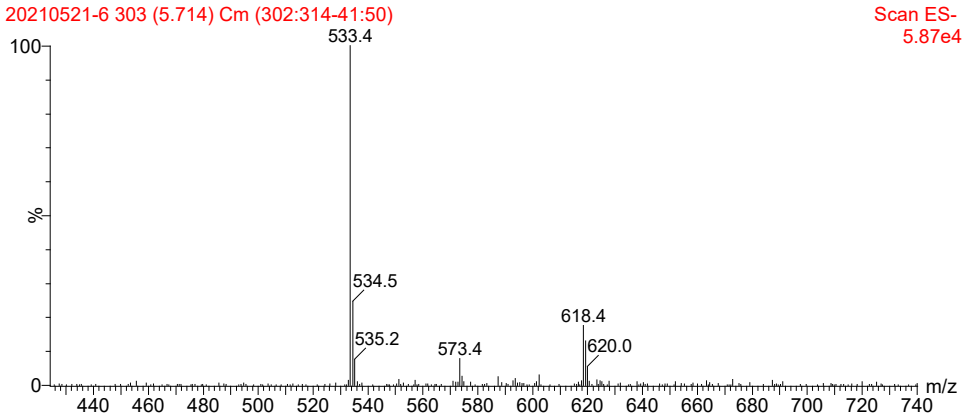

Supplementary Figure 4 ESI-MS spectrum for **S-HL** in CH_2Cl_2.

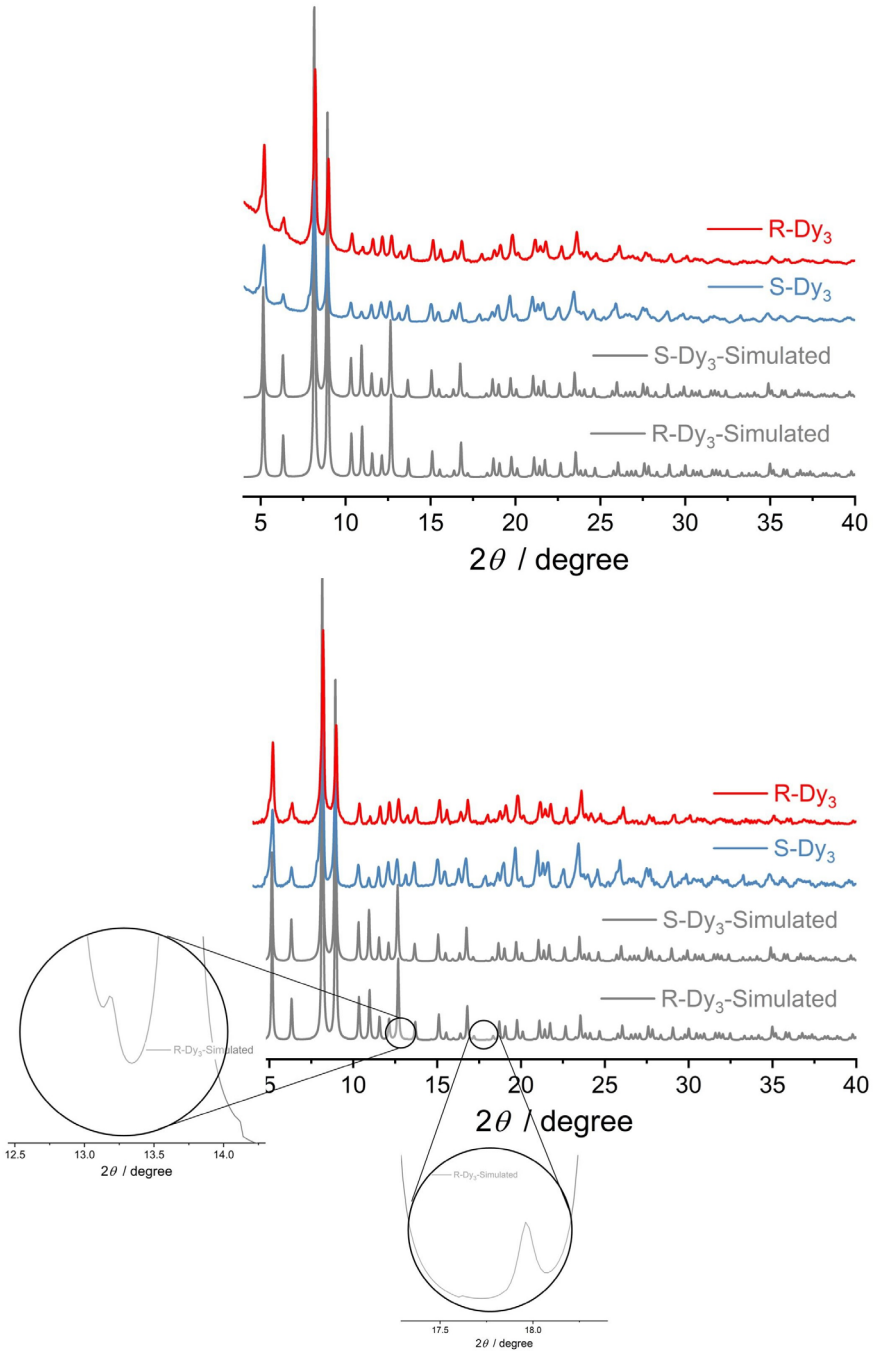

Supplementary Figure 5 Experimental (top, without baseline correction; bottom, with baseline correction) and simulated powder X-ray diffraction experiments for **R/S-Dy$_3$**. Note: the differences in diffraction peak intensities between experimental and simulated pattern may related to the crystal preferred orientation and the minor orientation alignments during PXRD sample preparation.[1]

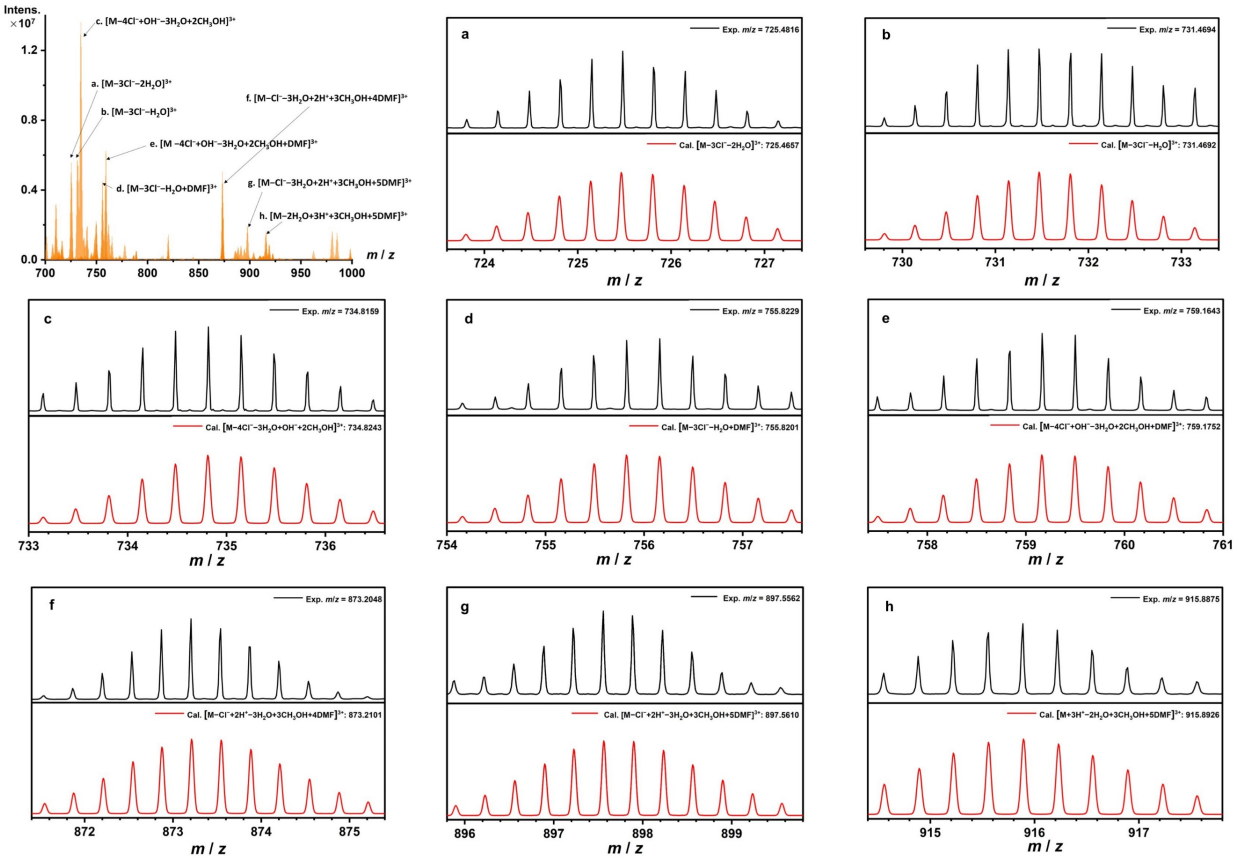

Supplementary Figure 6 High-resolution ESI-MS spectra of **R-Dy3** in CH_3OH (black line) and the corresponding simulated isotopic patterns (red line).

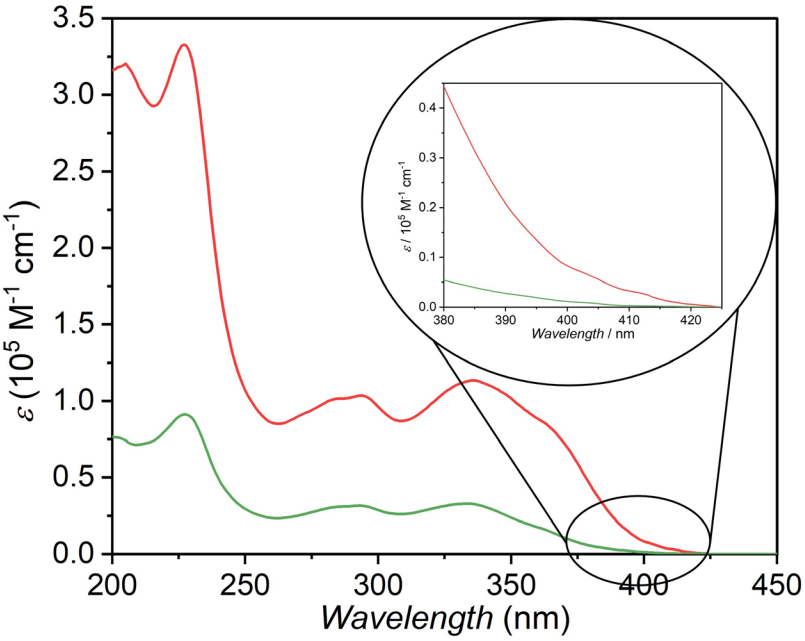

Supplementary Figure 7 UV-Vis absorption spectra of **R-HL** (green line) and **R-Dy$_3$** (red line) in CH_3OH ($c = 1 \times 10^{-5}$ M) at room temperature.

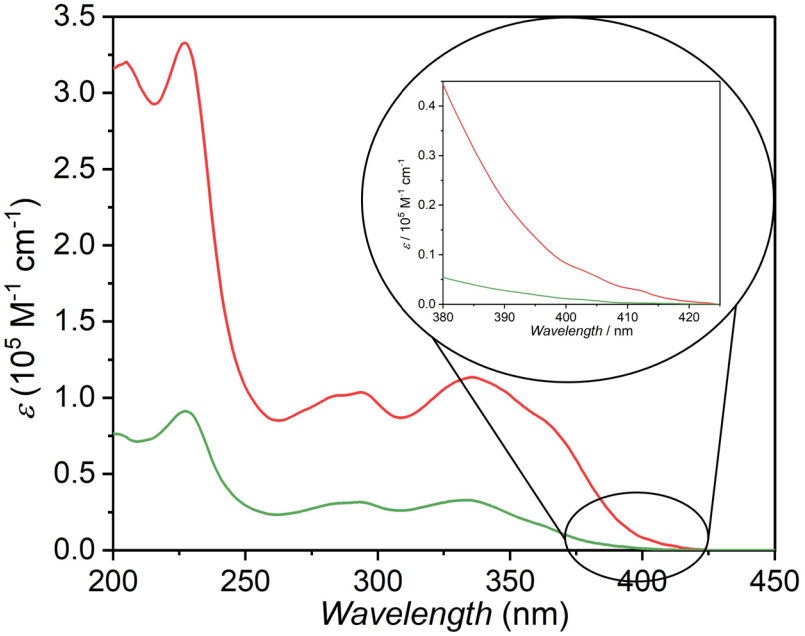

Supplementary Figure 8 UV-Vis absorption spectra of **S-HL** (green line) and **S-Dy$_3$** (red line) in CH_3OH ($c = 1 \times 10^{-5}$ M) at room temperature.

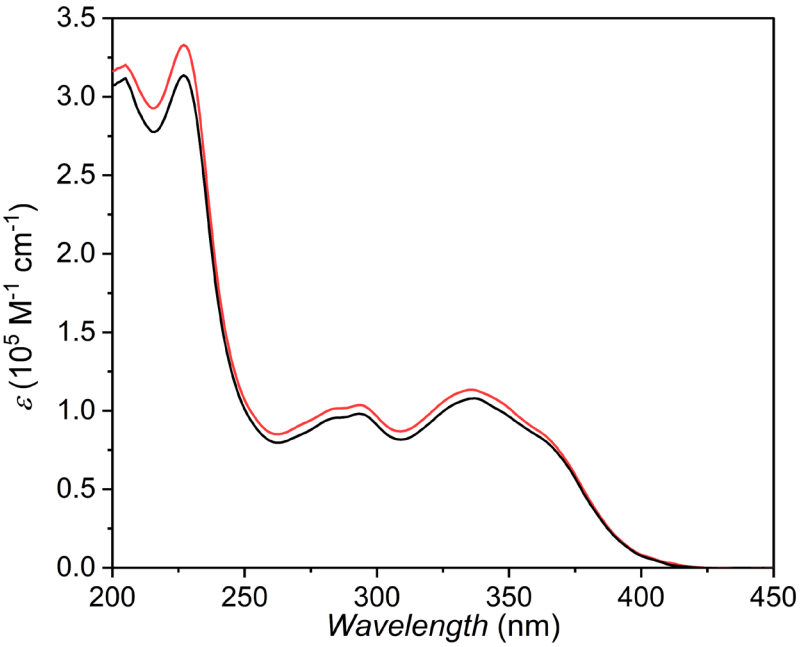

Supplementary Figure 9 UV-Vis absorption spectra of **R-Dy$_3$** (red line) and **S-Dy$_3$** (black line) in CH_3OH (c = 1.0 × 10^{-5} M) at room temperature.

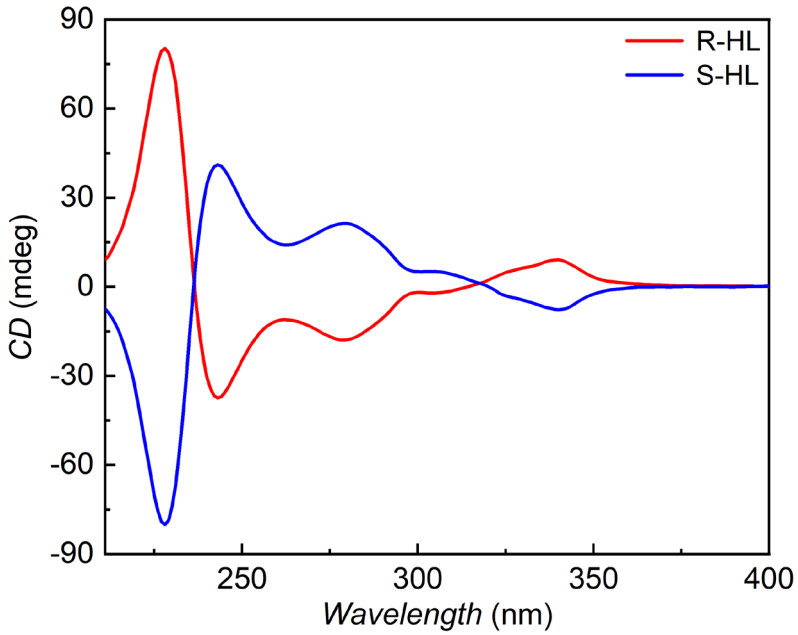

Supplementary Figure 10 NCD spectra of **R-HL** and **S-HL** in CH_3OH ($c = 2.0 \times 10^{-5}$ M) at room temperature.

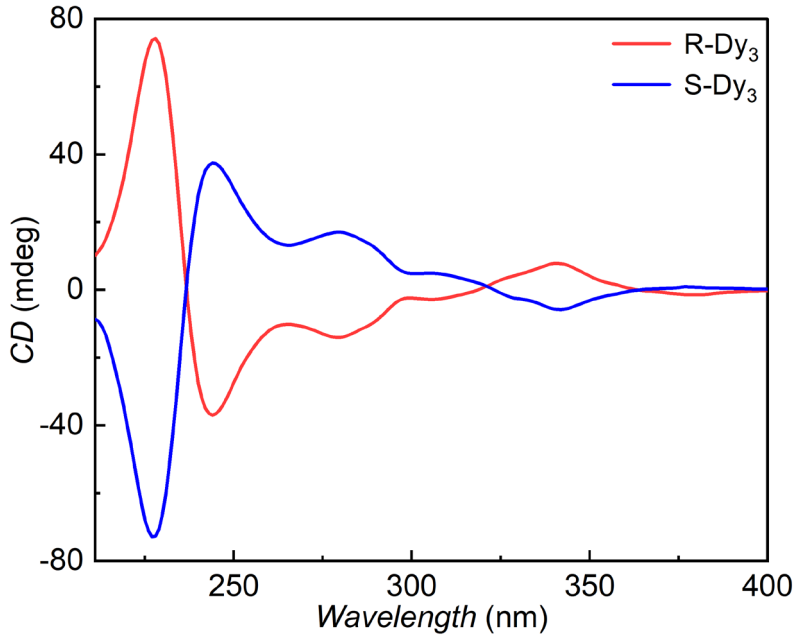

Supplementary Figure 11 NCD spectra of **R-Dy$_3$** and **S-Dy$_3$** in CH_3OH ($c = 6.6 \times 10^{-6}$ M) at room temperature.

2. Crystallography

The structures were solved by Intrinsic Phasing using SHELXT[2] and refined by Least Squares minimization using SHELXL[3] in OLEX2[4]. Non-hydrogen atoms in crystals were refined anisotropically. Hydrogen atoms were constrained to calculated positions and refined using the riding model. Because disordered solvent molecules cannot be modeled, a cleanly documented solvent mask was used. Crystallographic data can be obtained free of charge from the Cambridge Crystallographic Data Centre via www.ccdc.cam.ac.uk/data_request/cif and the deposition numbers of these data are CCDC 2323094 and 2323095. Crystallographic data, selected bond distances and bond angles are presented in Supplementary Tables 2-4.

Notes for B-level alerts in **R/S-Dy$_3$**:

R-Dy$_3$:

PLAT220_ALERT_2_B NonSolvent Resd 1 C Ueq(max)/Ueq(min) Range 7.1 Ratio. Please Check

Author Response: The alert is generated because there is some disorder in the structure. High thermal motion of OMe and OEt groups may exhibit such unusual ratios.

PLAT420_ALERT_2_B D-H Bond Without Acceptor O4-H4. Please Check

Author Response: Solvent molecules that should form hydrogen bonds have been removed by the SQUEEZE subroutine in the PLATON due to their highly disordered nature.

PLAT420_ALERT_2_B D-H Bond Without Acceptor O5-H5. Please Check

Author Response: Solvent molecules that should form hydrogen bonds have been removed by the SQUEEZE subroutine in the PLATON due to their highly disordered nature.

PLAT420_ALERT_2_B D-H Bond Without Acceptor O6-H6A. Please Check

Author Response: Solvent molecules that should form hydrogen bonds have been removed by the SQUEEZE subroutine in the PLATON due to their highly disordered nature.

PLAT420_ALERT_2_B D-H Bond Without Acceptor O6-H6B. Please Check

Author Response: Solvent molecules that should form hydrogen bonds have been removed by the SQUEEZE subroutine in the PLATON due to their highly disordered nature.

S-Dy$_3$:

PLAT420_ALERT_2_B D-H Bond Without Acceptor O4-H4. Please Check

Author Response: Solvent molecules that should form hydrogen bonds have been removed by the SQUEEZE subroutine in the PLATON due to their highly disordered nature.

PLAT420_ALERT_2_B D-H Bond Without Acceptor O5-H5A. Please Check

Author Response: Solvent molecules that should form hydrogen bonds have been removed by the SQUEEZE subroutine in the PLATON due to their highly disordered nature.

PLAT420_ALERT_2_B D-H Bond Without Acceptor O6-H6A. Please Check

Author Response: Solvent molecules that should form hydrogen bonds have been removed by the SQUEEZE subroutine in the PLATON due to their highly disordered nature.

PLAT420_ALERT_2_B D-H Bond Without Acceptor O6-H6B. Please Check

Author Response: Solvent molecules that should form hydrogen bonds have been removed by the SQUEEZE subroutine in the PLATON due to their highly disordered nature.

Supplementary Table 1 Representative single-molecule toroics and references.

Abbreciation	Space group	References
Dy_3-1	*C*2/c	*Angew. Chem. Int. Ed.*, **2006**, 1729
Dy_3-2	*P*na2_1	*Chem. Sci.*, **2012**, 3366
Dy_4-1	*P*4_2/n	*Angew. Chem. Int. Ed.*, **2018**, 17089
Dy_4-2	*C*2/c	*Chem. Commun.*, **2022**, 1784
Dy_6-1	*R*-3	*J. Am. Chem. Soc.*, **2012**, 18554
Dy_6-2	*P*-1	*Angew. Chem. Int. Ed.*, **2012**, 16767
Dy_6-3	*P*-1	*Angew. Chem. Int. Ed.*, **2010**, 6352
Dy_6-4	*P*-1	*Chem. Commun.*, **2016**, 9570
Dy_3Cu	*P*2_1	*Chem. Sci.*, **2012**, 1169
Dy_6Cr	*P*-1	*Nat. Commun.*, **2017**, 1023
Dy_8Fe_8	*P*n-3n	*Matter*, **2020**, 1481
Dy_6Fe_{18}	*P*ccn	*J. Am. Chem. Soc.*, **2020**, 14838
Tb_6Cu_6	*P*-3c1	*Chem. Commun.*, **2018**, 1065
Tb_4-1	*P*-1	*Inorg. Chem. Front.*, **2022**, 784
Tb_4-TC4A	*P*-1 or *C*2/c	*Chem. Sci.*, **2023**, 7208

Supplementary Table 2 Crystal data and structure refinement for **R-Dy3** and **S-Dy3**.

Compound reference	**R-Dy3**	**S-Dy3**
Chemical formula	$C_{126}H_{170}Cl_4N_{15}O_{35}Dy_3$	$C_{126}H_{170}Cl_4N_{15}O_{35}Dy_3$
Formula Mass	3084.06	3084.06
Crystal system	cubic	cubic
a (Å)	24.1722(6)	24.2358(9)
b (Å)	24.1722(6)	24.2358(9)
c (Å)	24.1722(6)	24.2358(9)
α (°)	90	90
β (°)	90	90
γ (°)	90	90
Unit cell volume (Å^3)	14123.7(11)	14235.5(16)
Temperature (K)	180.0	180.0
Space group	$P2_13$	$P2_13$
Z	4	4
ρ_{calc} (g/cm^3)	1.450	1.439
F (000)	6308.0	6308.0
Radiation	MoKα (λ = 0.71073)	MoKα (λ = 0.71073)
Reflections collected	78566	41369
Independent reflections	8348	8369
R_{int}	0.0992	0.1260
GOF on F^2	1.092	1.023
R_1 (I ≥2 σ (*I*))	0.0623	0.0660
wR_2 (all data)	0.1971	0.2205
Flack parameter	0.022(10)	0.025(12)
CCDC number	2323095	2323094

Supplementary Table 3 Selected bond distances (Å) for **R-Dy3** and **S-Dy3**.

R-Dy3		**S-Dy3**	
Dy1-O1	2.466(10)	Dy1-O1	2.467(12)
Dy1-O2	2.366(10)	Dy1-O2	2.356(13)
Dy1-O2^1	2.348(9)	Dy1-O2^2	2.376(11)
Dy1-O3^1	2.283(12)	Dy1-O3^2	2.292(16)
Dy1-O4	2.333(11)	Dy1-O4	2.3251(11)
Dy1-O5	2.3069(8)	Dy1-O5	2.343(13)
Dy1-O6	2.3591(10)	Dy1-O6	2.3733(13)
Dy1-Cl1	2.598(8)	Dy1-Cl1	2.619(9)
Dy1-Dy1^1	3.5113(13)	Dy1-Dy1^1	3.5220(16)

Supplementary Table 4 Selected bond angles (°) for **R-Dy$_3$** and **S-Dy$_3$**.

R-Dy$_3$		**S-Dy$_3$**	
Dy1^1-Dy1-Dy1^2	60.0	Dy1^1-Dy1-Dy1^2	60.0
Dy1-O2-Dy1^1	96.3(3)	Dy1-O2-Dy1^1	96.2(4)
Dy1-O4-Dy1^1	97.6(6)	Dy1-O4-Dy1^1	97.5(7)
Dy1-O5-Dy1^1	99.11(3)	Dy1-O5-Dy1^1	98.47(4)
O1-Dy1-Cl1	80.7(4)	O1-Dy1-Cl1	81.0(4)
O2-Dy1-Cl1	102.3(4)	O2-Dy1-Cl1	102.4(4)
O2-Dy1-O1	63.2(3)	O2-Dy1-O1	62.5(4)
O2^1-Dy1-Cl1	91.4(3)	O2^1-Dy1-Cl1	92.5(4)
O2^1-Dy1-O1	153.0(4)	O2^1-Dy1-O1	153.5(4)
O2^1-Dy1-O2	143.7(3)	O2^1-Dy1-O2	143.7(4)
O2^1-Dy1-O6	103.9(3)	O2^1-Dy1-O6	103.3(4)
O3^1-Dy1-Cl1	83.1(7)	O3^1-Dy1-Cl1	83.0(6)
O3^1-Dy1-O1	83.0(4)	O3^1-Dy1-O1	81.9(5)
O3^1-Dy1-O2	143.9(4)	O3^1-Dy1-O2	142.2(5)
O3^1-Dy1-O2^1	70.4(4)	O3^1-Dy1-O2^1	71.8(5)
O3^1-Dy1-O4	141.2(4)	O3^1-Dy1-O4	142.0(4)
O3^1-Dy1-O5	124.7(6)	O3^1-Dy1-O5	125.4(5)
O3^1-Dy1-O6	74.2(6)	O3^1-Dy1-O6	74.2(5)
O4-Dy1-Cl1	81.1(5)	O4-Dy1-Cl1	80.8(6)
O4-Dy1-O1	128.5(3)	O4-Dy1-O1	128.5(4)
O4-Dy1-O2	74.4(3)	O4-Dy1-O2	75.2(3)
O4-Dy1-O2^1	74.8(3)	O4-Dy1-O2^1	74.8(3)
O4-Dy1-O6	131.8(5)	O4-Dy1-O6	132.0(5)
O5-Dy1-Cl1	138.93(17)	O5-Dy1-Cl1	139.23(19)
O5-Dy1-O1	127.6(3)	O5-Dy1-O1	127.0(3)
O5-Dy1-O2	73.7(2)	O5-Dy1-O2	73.8(3)
O5-Dy1-O2^1	74.0(3)	O5-Dy1-O2^1	73.4(3)
O5-Dy1-O4	58.2(5)	O5-Dy1-O4	58.8(6)
O5-Dy1-O6	74.93(3)	O5-Dy1-O6	74.47(4)
O6-Dy1-Cl1	146.07(17)	O6-Dy1-Cl1	146.19(18)
O6-Dy1-O1	71.9(3)	O6-Dy1-O1	71.5(4)
O6-Dy1-O2	83.2(3)	O6-Dy1-O2	82.3(4)

Supplementary Table 5 The CShM values calculated by SHAPE 2.1 for **R-Dy$_3$** and **S-Dy$_3$**.

Central atom	Coordination Geometry	**R-Dy$_3$**	**S-Dy$_3$**
Dy	Hexagonal bipyramid (D_{6h})	15.767	15.796
	Cube (O_h)	11.237	11.301
	Square antiprism (D_{4d})	2.197	2.237
	Triangular dodecahedron (D_{2d})	1.414	1.389
	Johnson gyrobifastigium J26 (D_{2d})	15.219	15.205
	Johnson elongated triangular bipyramid J14 (D_{3h})	28.244	28.526
	Biaugmented trigonal prism J50 (C_{2v})	3.455	3.496
	Biaugmented trigonal prism (C_{2v})	2.654	2.632
	Snub diphenoid J84 (D_{2d})	4.319	4.280

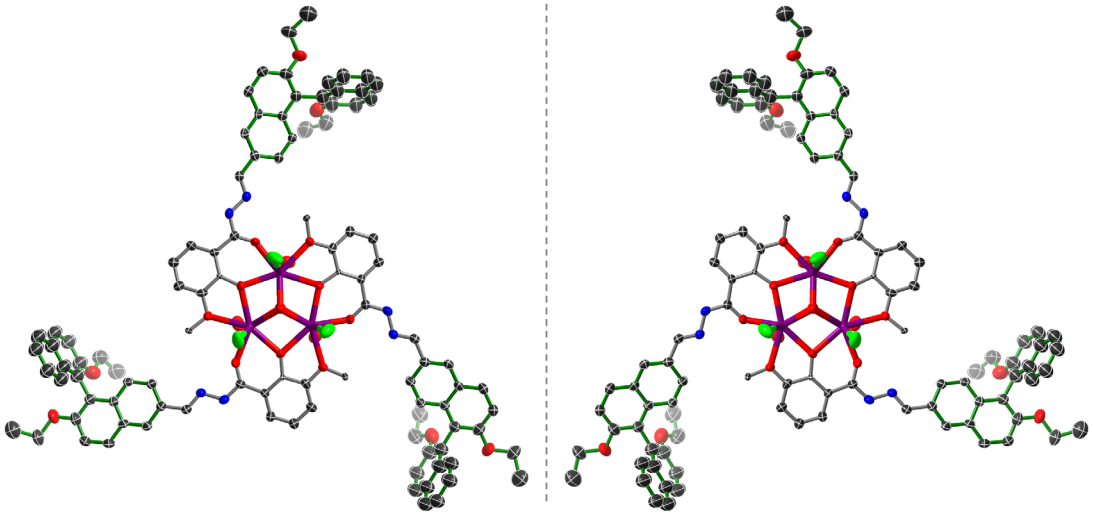

Supplementary Figure 12 Molecular structures of **R-Dy$_3$** (left, CCDC 2323095) and **S-Dy$_3$** (right, CCDC 2323094). Non-coordinating anions and solvent molecules as well as hydron atoms are omitted for clarity. Thermal ellipsoids set at 30% probability. Color codes: violet, Dy; red, O; green, Cl; black, C.

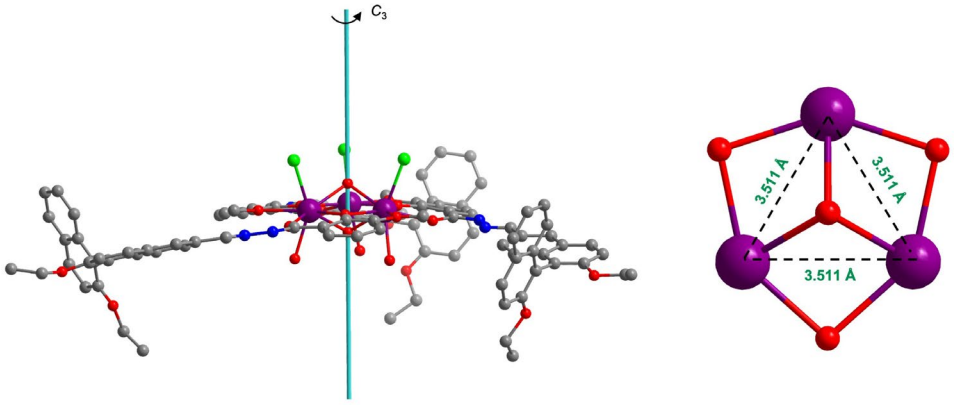

Supplementary Figure 13 The three-fold axis of rotation in **R-Dy$_3$** (left) and the Dy$_3$ core with equilateral triangle geometry configuration (right).

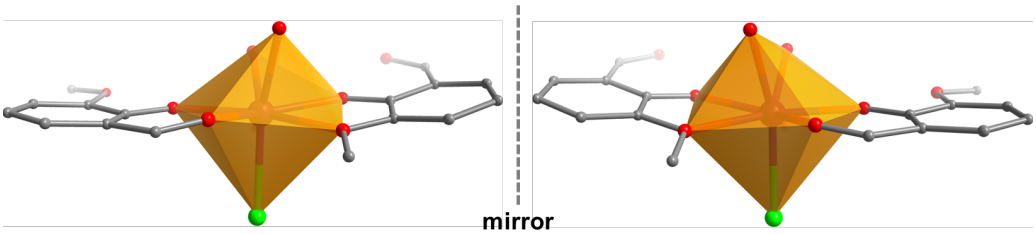

Supplementary Figure 14 The first coordination environment of Dy(III) in **R-Dy$_3$** (right) and **S-Dy$_3$** (left). Color codes: violet, Dy; red, O; green, Cl; grey, C.

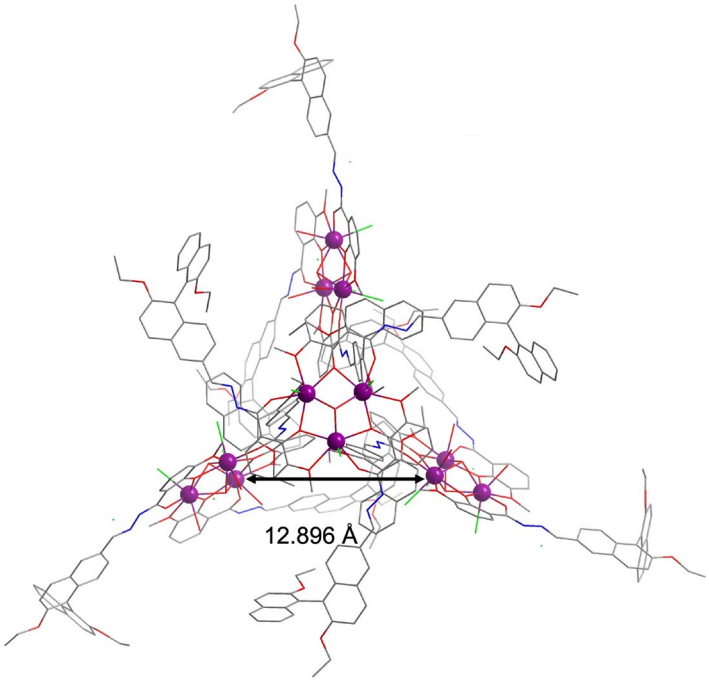

Supplementary Figure 15 The packing diagram for **R-Dy$_3$** shown along the crystallographic *c* axis gives the shortest intermolecular Dy···Dy distance of 12.896 Å. Color codes: violet, Dy; red, O; green, Cl; blue, N; grey, C.

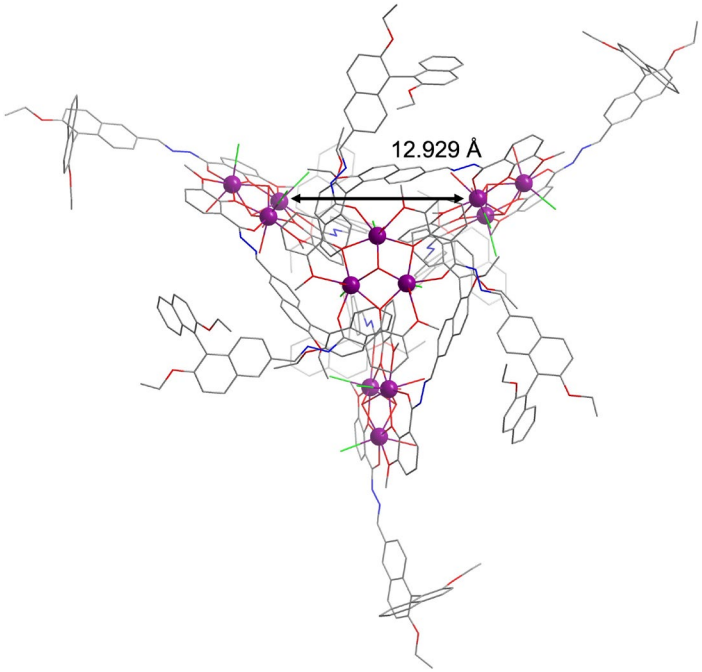

Supplementary Figure 16 The packing diagram for **S-Dy$_3$** shown along the crystallographic *c* axis gives the shortest intermolecular Dy···Dy distance of 12.929 Å. Color codes: violet, Dy; red, O; green, Cl; blue, N; grey, C.

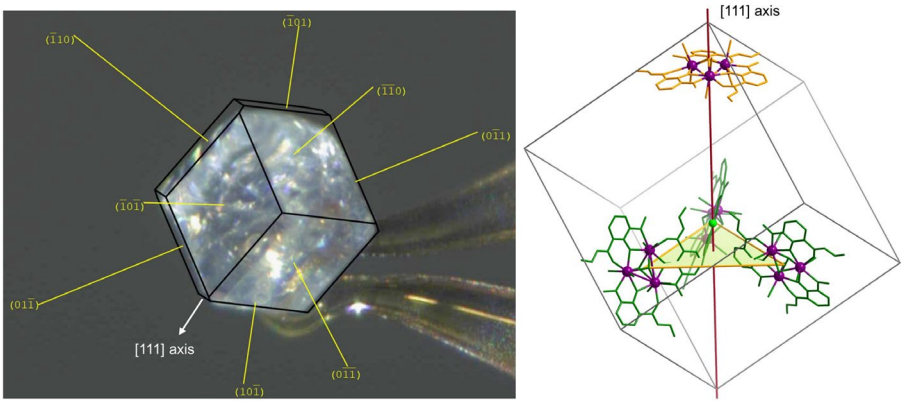

Supplementary Figure 17 The single-crystal facets assignment for **R-Dy$_3$** with indication of [111] direction (left) and the corresponding structural view (right). The BINOL derivates are omitted for clarity. The (111) plane is perpendicular to [111] axis.

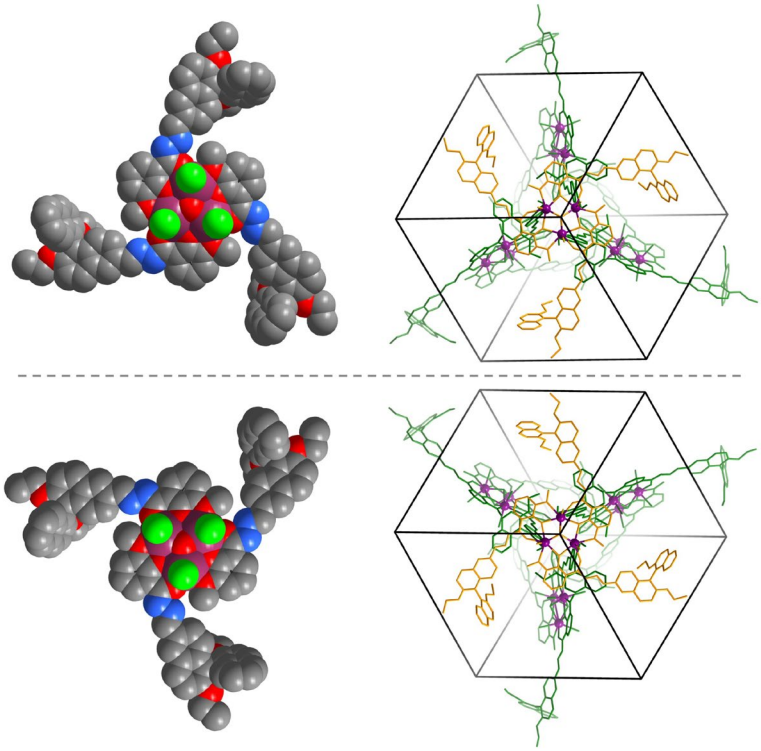

Supplementary Figure 18 Propeller-shaped molecular (left) and supramolecular (right) chirality in **R-Dy$_3$** (top) and **S-Dy$_3$** (bottom), respectively. This system exhibits four types of chiral features: i) local axial chirality from the functionalized BINOL ligands, ii) propeller molecular chirality from clockwise (P) or anticlockwise (M) arrangement of hydrazide-modified o-vanillin around Dy(III) ion, iii) supramolecular propeller chirality formed through the weak intermolecular C/N-H···Cl interactions among three trimers and iv) spin chirality of the magnetic easy axes of the Dy(III) ions in the triangular trimer (Fig. 2d).

3. Magnetic measurements

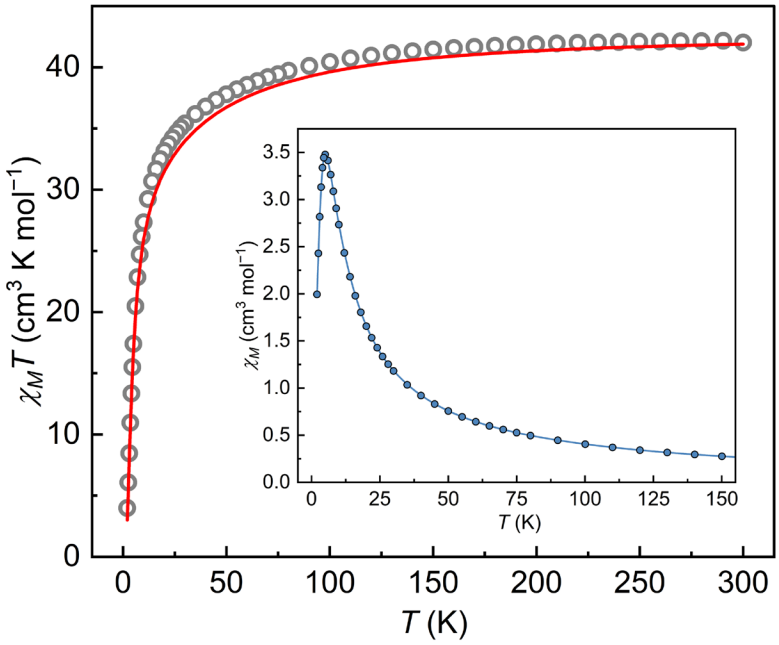

Supplementary Figure 19 The $\chi_M T$ vs. T (inset: χ_M vs. T) plots for **R-Dy$_3$**. The red line represents the calculated results from CASPT2/SO with J of -0.22 cm^{-1}.

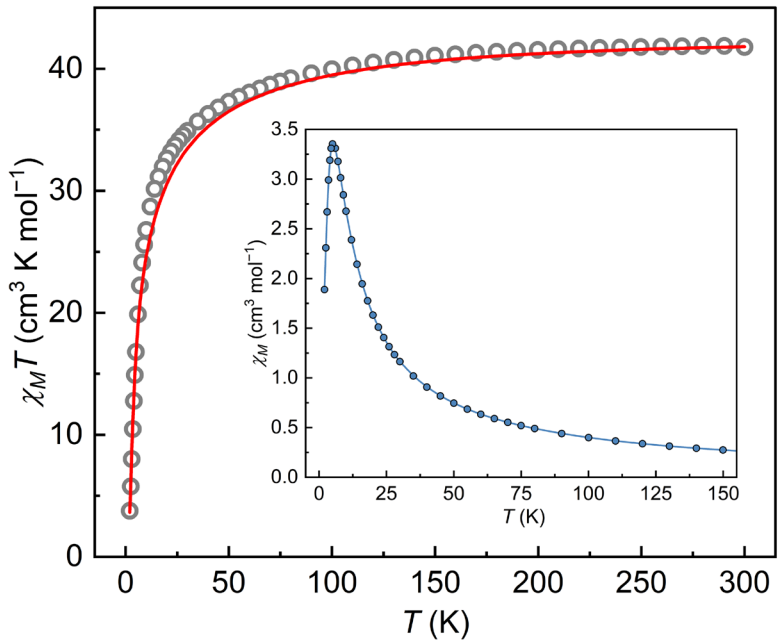

Supplementary Figure 20 The $\chi_M T$ vs. T (inset: χ_M vs. T) plots for **S-Dy$_3$**. The red line represents the calculated results from CASPT2/SO with J of -0.405 cm^{-1}.

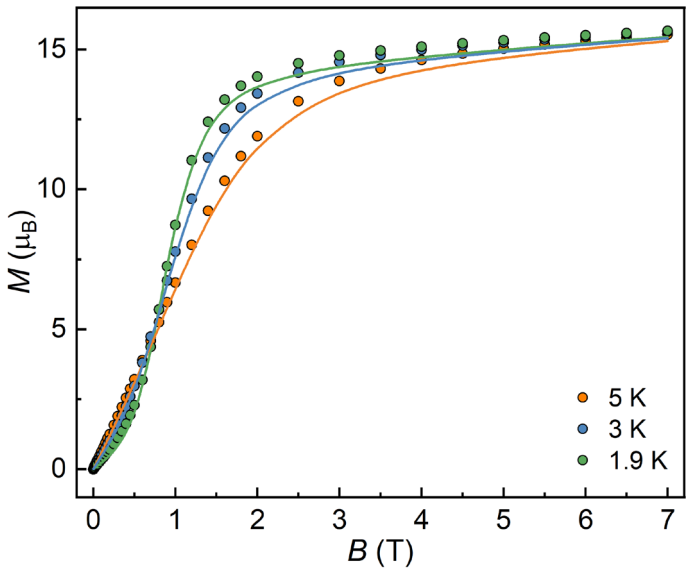

Supplementary Figure 21 Field dependence of magnetization at different temperatures for **R-Dy$_3$**. Experimental data (symbols) are compared with the calculated molar magnetization (solid lines) by CASPT2/SO.

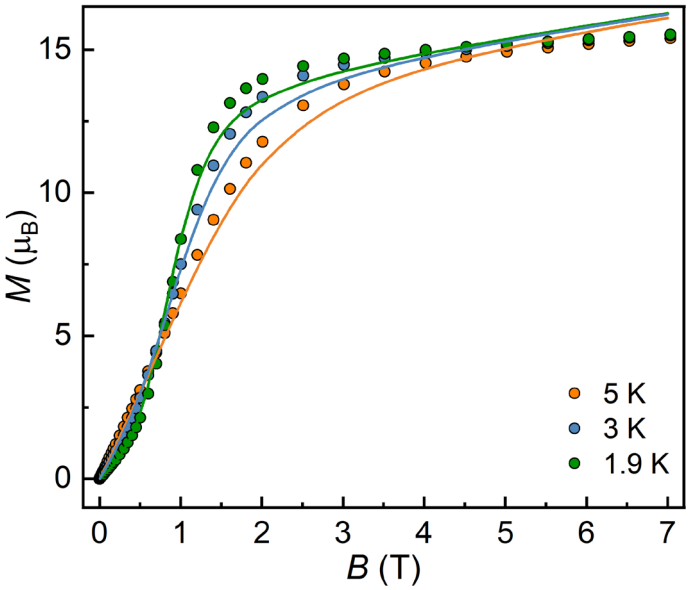

Supplementary Figure 22 Field dependence of magnetization at different temperatures for **S-Dy$_3$**. Experimental data (symbols) are compared with the calculated molar magnetization (solid lines) by CASPT2/SO. Note that the differences in the calculated plots between **R-Dy$_3$** and **S-Dy$_3$** mainly arise from subtle differences in the first coordination environment of Dy(III) ion (Supplementary Table 3)[5]. Due to Zeeman mixing, the lower energy excited states of **S-Dy$_3$** (Supplementary Table 8) contribute more to the high-field magnetization than those of **R-Dy$_3$**. However, the simulated magnetization curves for them in the low-field region are highly superimposable and both exhibit excellent agreement with the experimental data. Combined with the *ab initio* results, the S-shaped magnetization curves strongly confirmed the toroidal ground state in these two compounds.

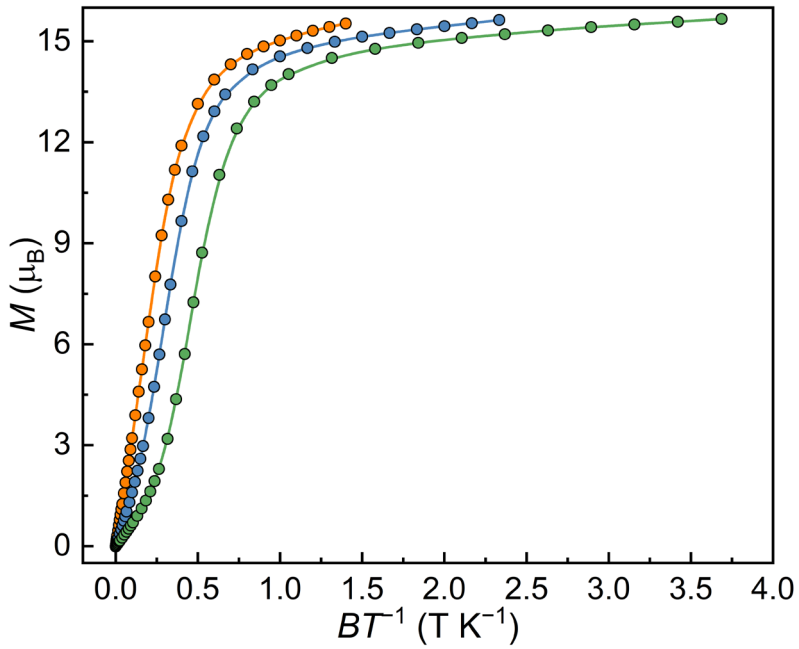

Supplementary Figure 23 *M* vs. *B*/*T* plots for **R-Dy$_3$**. Green line, 1.9 K; blue line, 3.0 K; orange line, 5.0 K. The solid lines are guides for the eye.

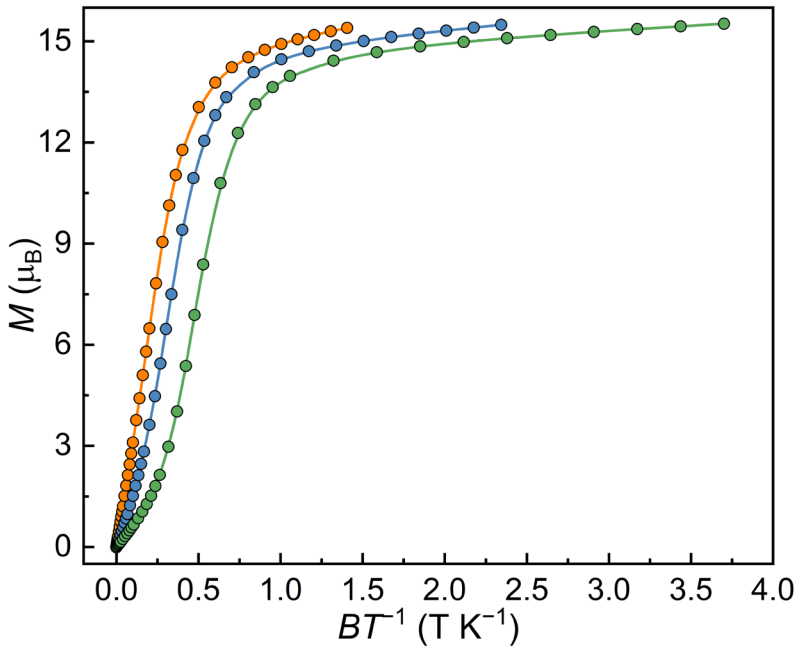

Supplementary Figure 24 *M* vs. *B*/*T* plots for **S-Dy$_3$**. Green line, 1.9 K; blue line, 3.0 K; orange line, 5.0 K. The solid lines are guides for the eye.

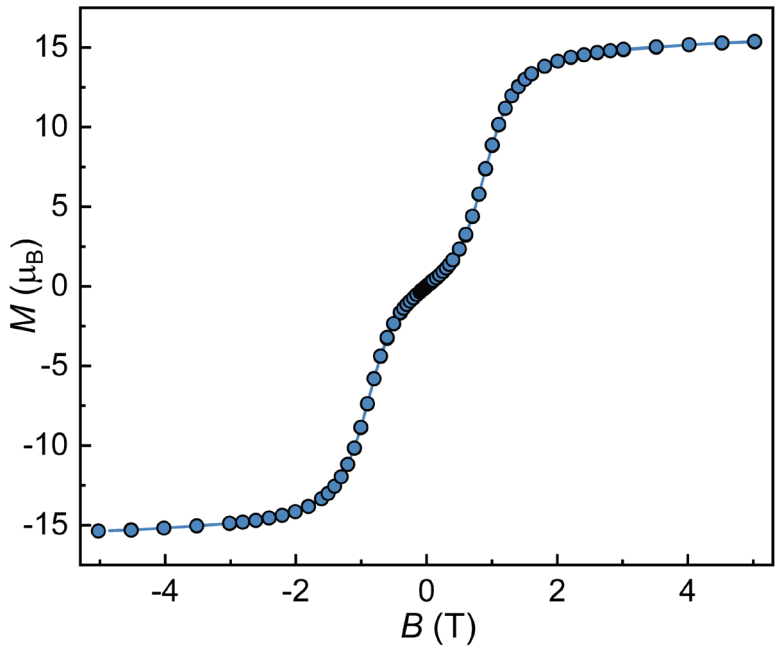

Supplementary Figure 25 Magnetic hysteresis loops of **R-Dy$_3$** at 1.9 K.

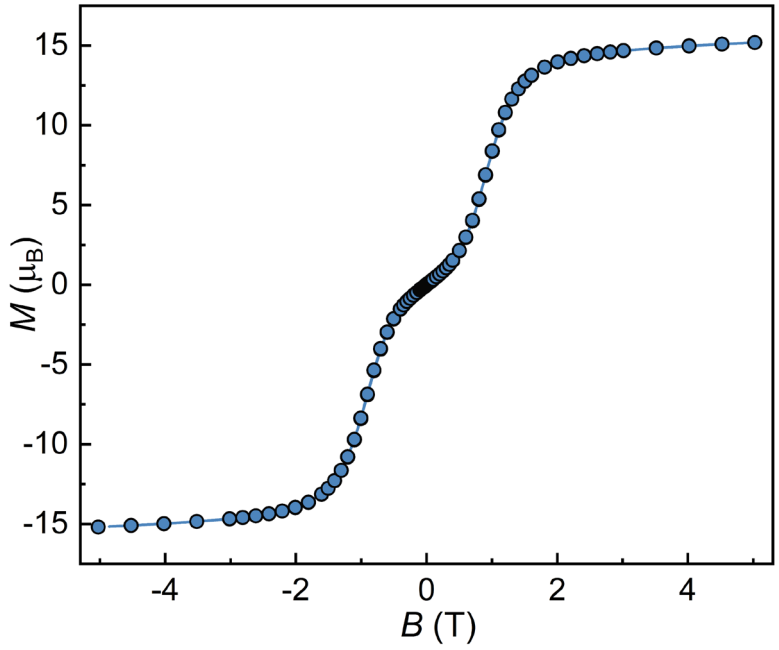

Supplementary Figure 26 Magnetic hysteresis loops of **S-Dy$_3$** at 1.9 K.

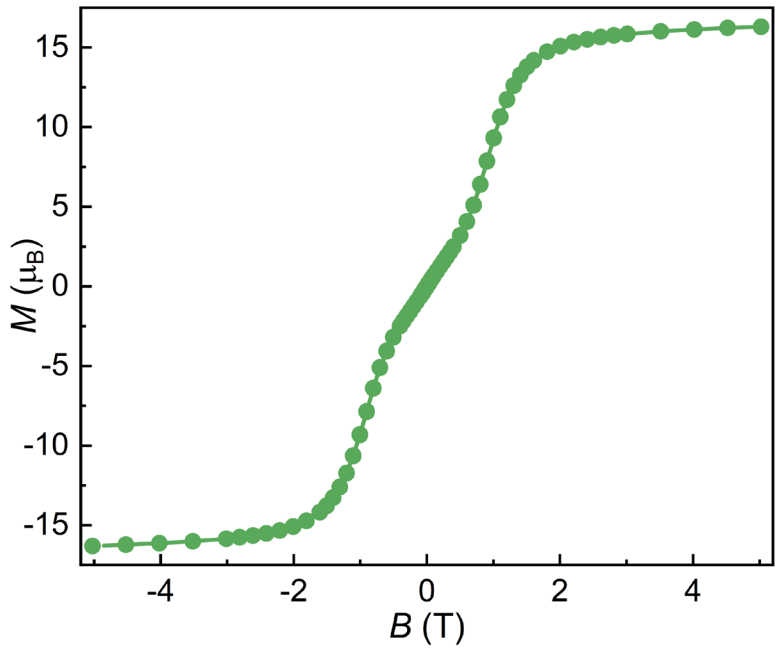

Supplementary Figure 27 Magnetic hysteresis loops of **R-Dy$_3$** in CH_3OH (c = 8.3 mM) collected at 1.9 K.

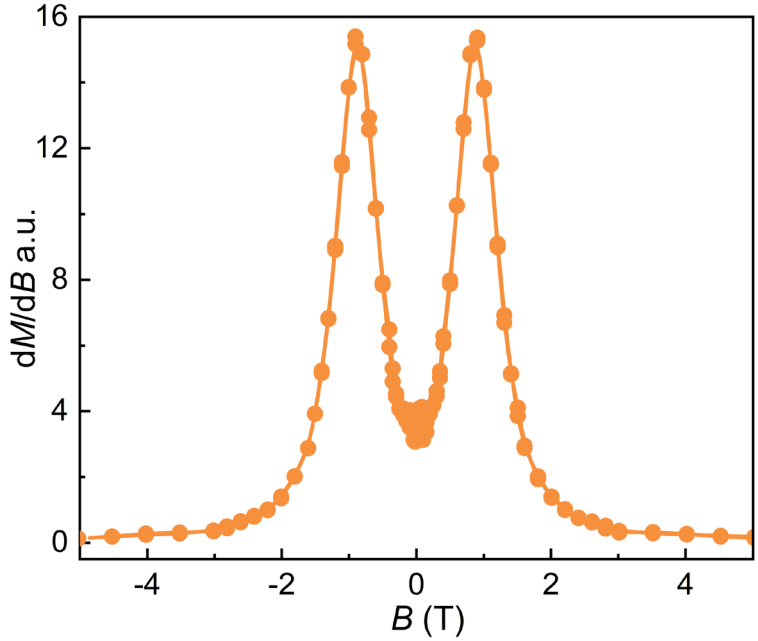

Supplementary Figure 28 dM/dH for **R-Dy$_3$** at 1.9 K.

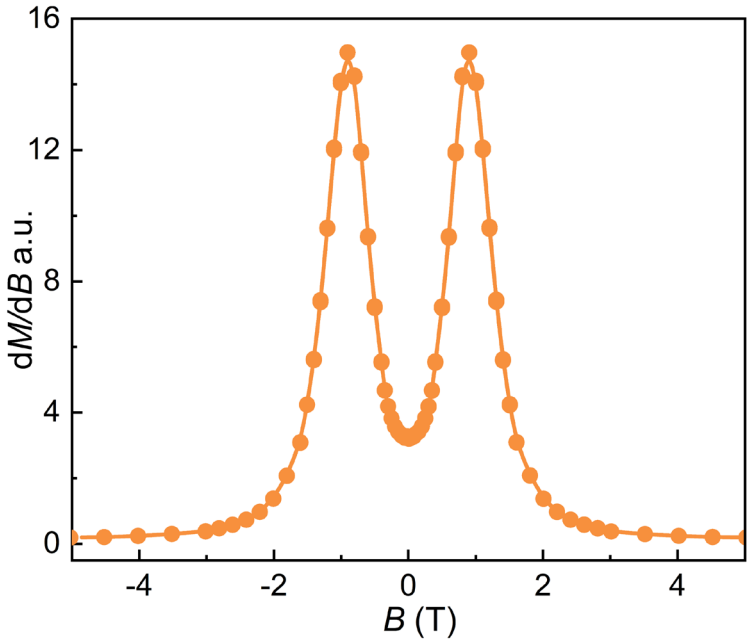

Supplementary Figure 29 d*M*/d*H* for **S-Dy$_3$** at 1.9 K.

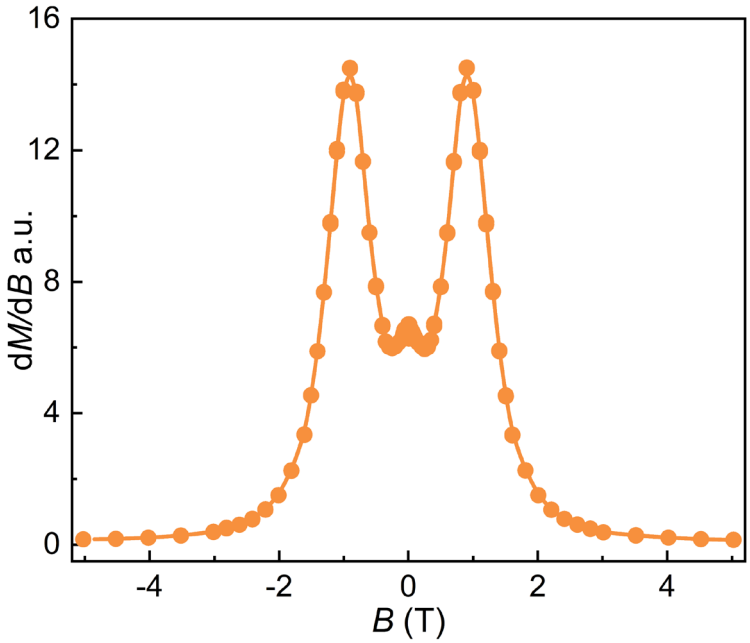

Supplementary Figure 30 d*M*/d*H* for **R-Dy$_3$** at 1.9 K in CH_3OH solution (c = 8.3 mM).

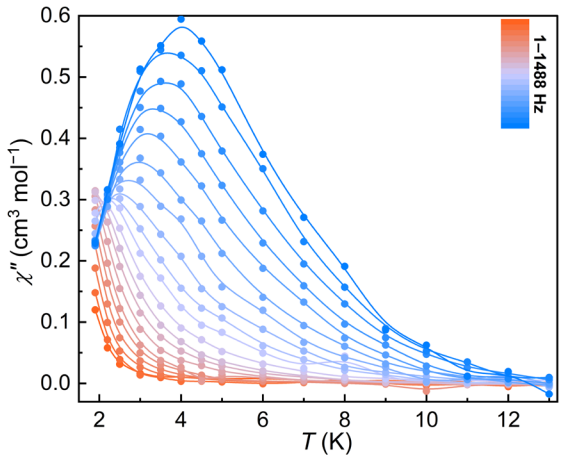

Supplementary Figure 31 Temperature-dependent out-of-phase ac magnetic susceptibilities for **R-Dy3** under a zero dc field at ac frequencies of 1–1488 Hz.

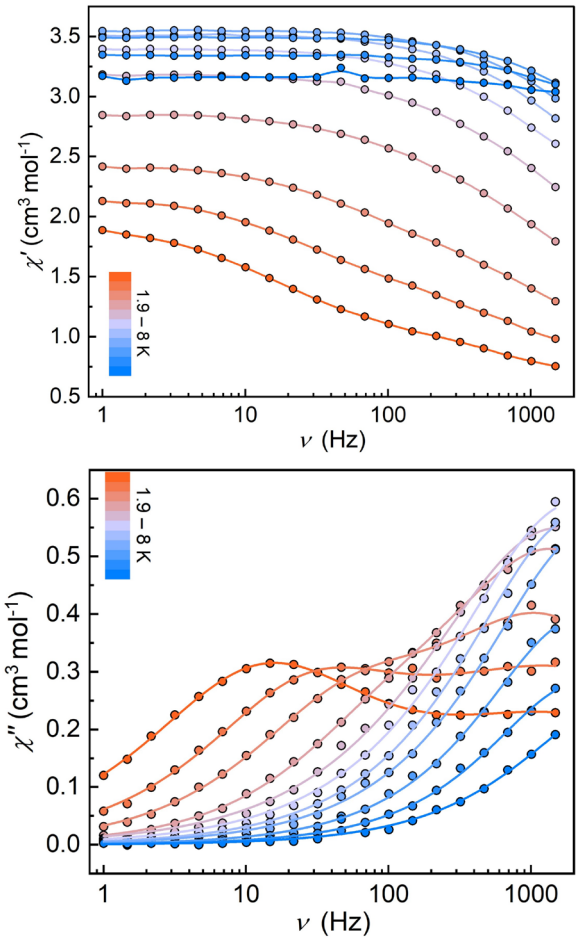

Supplementary Figure 32 Frequency-dependent in-phase (top) and out-of-phase (bottom) magnetic susceptibilities for **R-Dy3** under a zero dc field in the temperature range of 1.9 to 8.0 K. The solid lines in $\chi''(\upsilon)$ represent the fit via a two-step relaxation model from 1.9 to 3.0 K and a single relaxation process above 3.0 K.

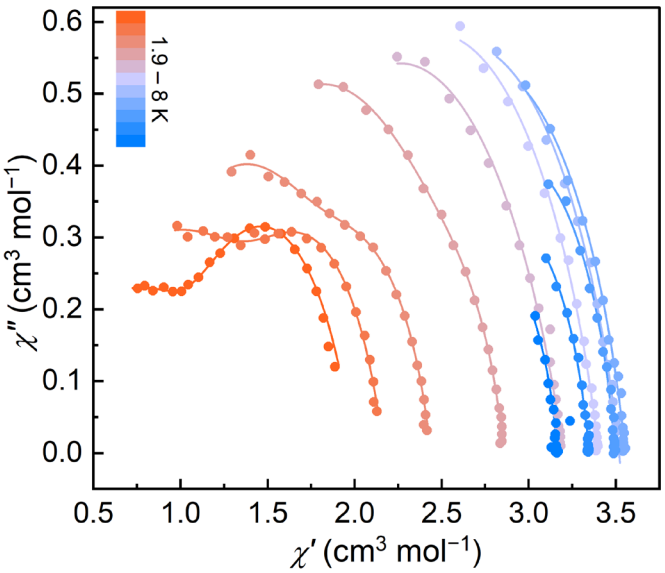

Supplementary Figure 33 Cole-Cole diagram for **R-Dy$_3$** at ac frequencies of 1–1488 Hz in the temperature range of 1.9 to 8.0 K. The solid lines represent the best fit obtained with the sum of two modified Debye functions between 1.9 and 3.0 K and a generalized Debye model above 3.0 K.

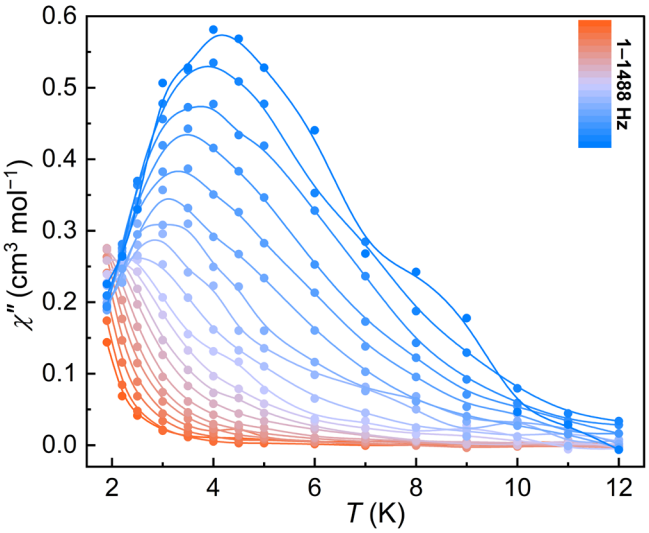

Supplementary Figure 34 Temperature-dependent out-of-phase ac magnetic susceptibilities for **S-Dy$_3$** under a zero dc field at ac frequencies of 1–1488 Hz.

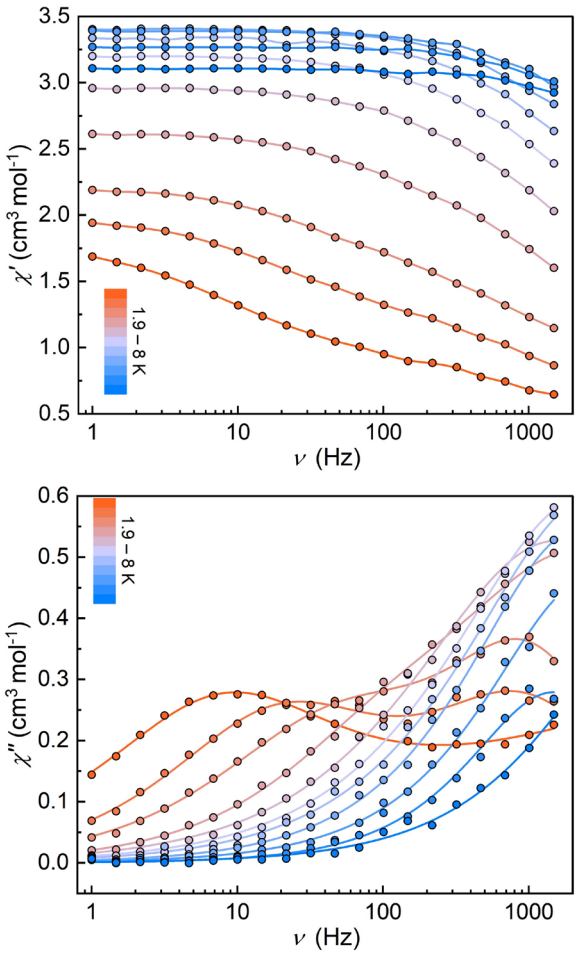

Supplementary Figure 35 Frequency-dependent in-phase (top) and out-of-phase (bottom) magnetic susceptibilities for **S-Dy3** under a zero dc field in the temperature range of 1.9 to 8.0 K. The solid lines in $\chi''(\upsilon)$ represent the fit via a two-step relaxation model from 1.9 to 3.0 K and a single relaxation process above 3.0 K.

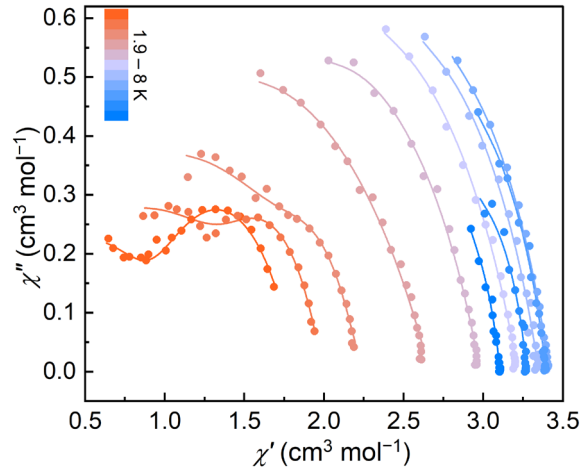

Supplementary Figure 36 Cole-Cole diagram for **S-Dy3** at ac frequencies of 1–1488 Hz in the temperature range of 1.9 to 8.0 K. The solid lines represent the best fit obtained with the sum of two modified Debye functions between 1.9 and 3.0 K and a generalized Debye model above 3.0 K.

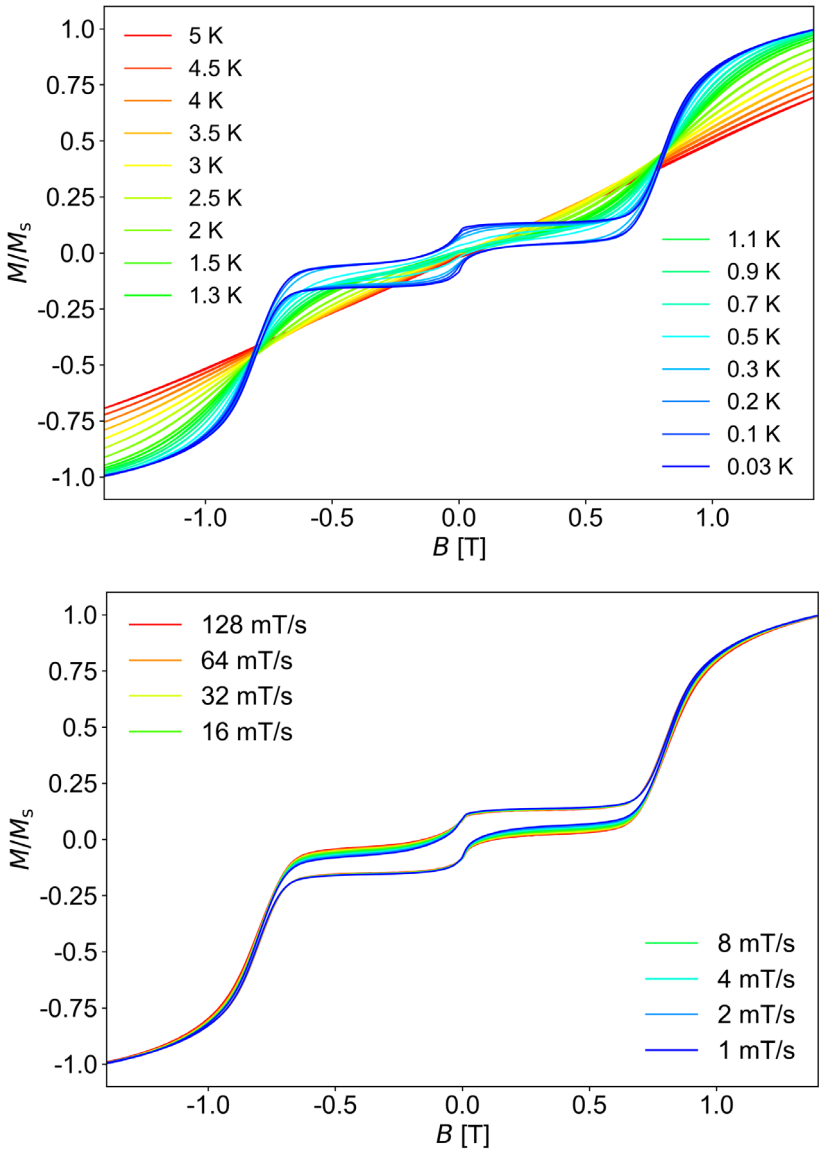

Supplementary Figure 37 μ-SQUID studies: magnetic hysteresis in the temperature range of 30 mK–5 K at 8 mT/s (top) and at 30 mK with different field sweep rates (bottom) for **S-Dy3**.

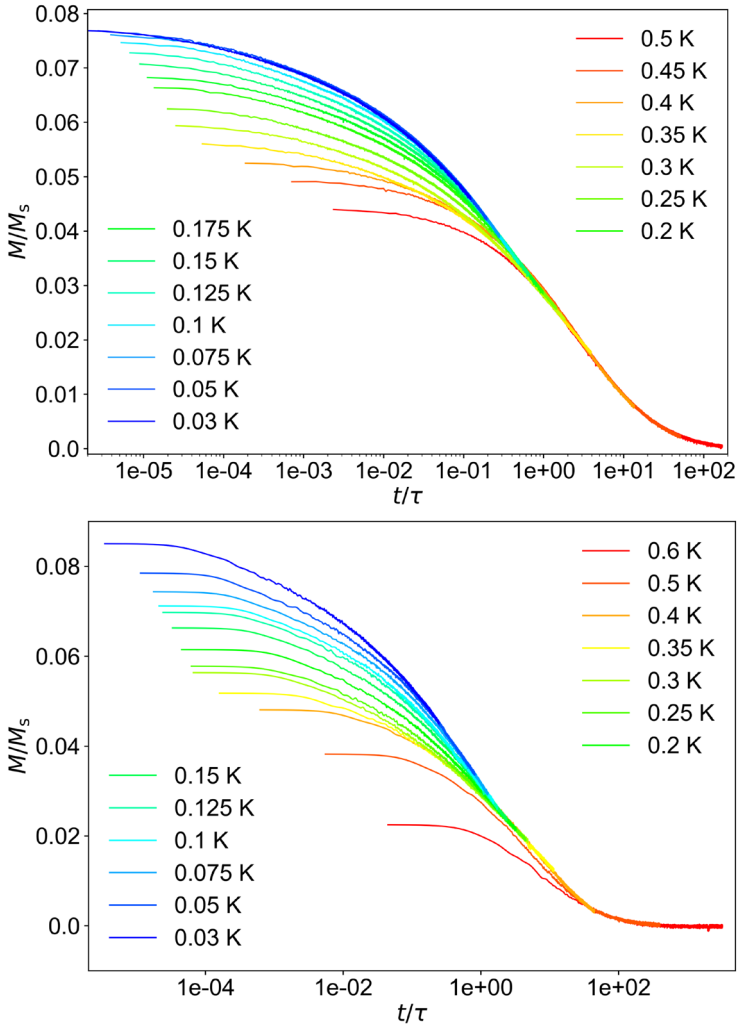

Supplementary Figure 38 Time dependent decay of magnetization at different temperatures for **R-Dy$_3$** (top) and **S-Dy$_3$** (bottom) measured by μ-SQUIDs. The magnetization after a field sweep (from above saturation ~ 1.4 T, to zero field) is first plotted as a function time ($M(t)$). The $M(t)$ curves at higher temperatures were rescaled to obtain a master curve corresponding to the lowest temperature. Its 1/e point provides the mean time at lowest temperature, while the individual scaling of time axis provides the relative mean times at higher temperatures. Eventually the master curve with non-dimensionalized (t/τ) axis, see $M = M_0/e$ at $t = \tau$, is shown here.

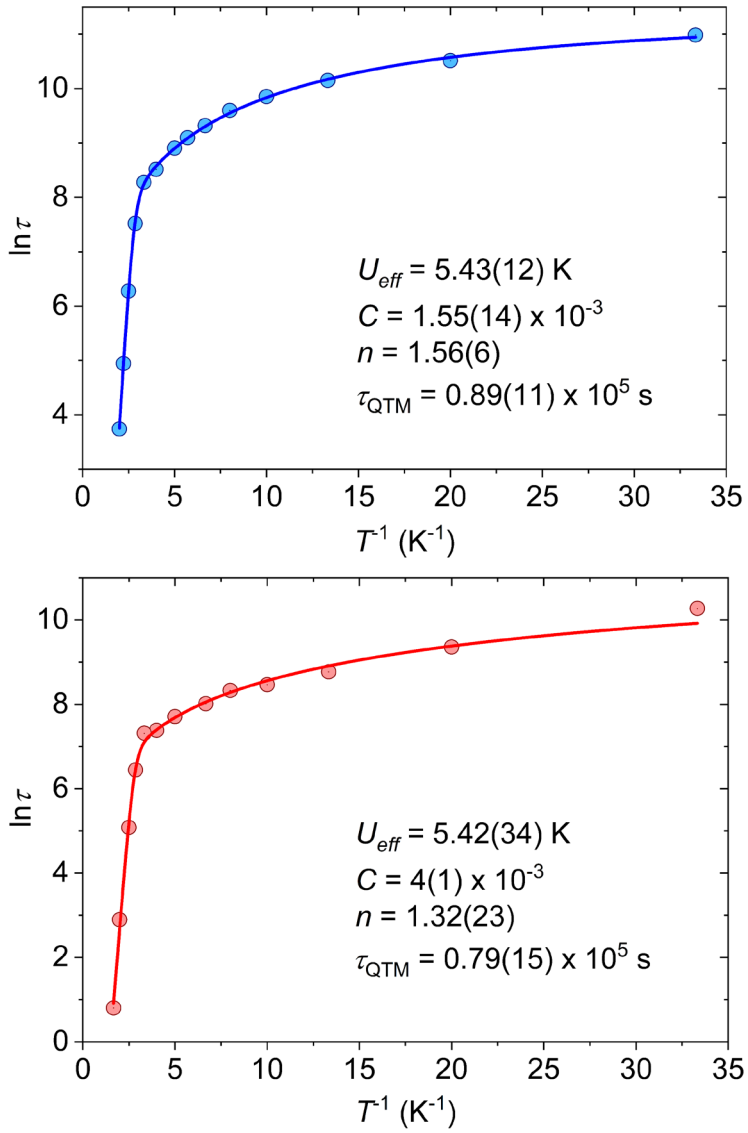

Supplementary Figure 39 Temperature dependence of the relaxation time in the form of natural logarithm for **R-Dy3** (top) and **S-Dy3** (bottom) obtained using μ-SQUIDs (see Supplementary Figure 38 caption). The solid lines represent the best fit to the expression $\ln(\tau) = -\ln[\tau_0^{-1}\exp(-U_{eff}/k_BT) + CT^n + 1/\tau_{QTM}]$ where τ_0 and U_{eff} are the parameters of Orbach process, C and n are the parameters for Raman relaxation and τ_{QTM} is the quantum tunnelling time, giving U_{eff} = 5.43(12) K, τ_0 = 8(2) × 10^{-4} s, C = 1.55(14) × 10^{-3} S^{-1} K^{-n}, n = 1.56(6) and τ_{QTM} = 0.89(11) × 10^5 s with adjusted R^2 = 0.999 for **R-Dy3** and U_{eff} = 5.42(34) K, τ_0 = 3(1) × 10^{-4} s, C = 4(1) × 10^{-3} S^{-1} K^{-n}, n = 1.32(23) and τ_{QTM} = 0.79(15) × 10^5 s with adjusted R^2 = 0.995 for **S-Dy3**, respectively.

4. *Ab initio* calculations

Computational details: The crystal structure of the **R/S-Dy3** molecules served this purpose. Given the exact C_3 point group symmetry of the investigated molecules, only one Dy site of each investigated molecule was computed by substituting the other two Dy sites with diamagnetic Lu ions. While this approach excludes the magnetic interaction effects between Dy sites on orbital optimization, we consider this influence negligible. Scalar relativistic corrections were accounted for in two steps based on the Douglas-Kroll-Hess approximation.[6-8] In the first step, scalar relativistic corrections are included in the employed basis sets for all atoms and are used to compute all mono- and bi-electronic repulsion integrals. To this end, all atoms were represented using ANO-RCC basis sets, which include scalar relativistic correction.[9-11] Cholesky decomposition of the bielectronic integrals was employed to save disk space and speed up the calculations.[12, 13] Electron repulsion integrals are further used to evaluate the energy and wave functions through the complete active space self-consistent field calculations (CASSCF). In this approach, all electronic states (roots) arising from the active space of the $4f^9$ configuration of the Dy(III), CAS(9 in 7), were optimised in state-average calculation. As such, 21 roots S = 5/2, 128 roots S = 3/2, and 130 roots S = 1/2 were mixed by the spin-orbit coupling, representing the second step of accounting for the relativistic effects.[14, 15] This approach accounts for the spin-orbit interaction in the mean-field approximation.[15] Dynamic electron correlation was added using the extended multistate multiconfigurational second-order perturbation theory (XMS-CASPT2) method,[6, 16-18] which not only corrects the diagonal energies of the spin-free states but also evaluates the effect of the second-order perturbation on the off-diagonal elements of the effective Hamiltonian. SINGLE_ANISO used the *ab initio* eigenstates and elements of the magnetic dipole moment to evaluate the magnetic properties, such as *g*-tensor for the ground and excited Kramers doublet states,[19, 20] magnetic susceptibility, molar magnetization, and crystal field splitting of the ground atomic *J*- multiplet.[21]

The magnetic exchange between Dy sites was described within the Lines model.[22] The dipolar coupling (the long-range interaction between magnetic moments) between Dy^{III} ions is routinely calculated as implemented in the POLY_ANISO code.[17, 23-25]

$$\widehat{H}_{total} = \widehat{H}_{exch} + \widehat{H}_{dip}$$

$$\widehat{H}_{exch} = -J(\hat{s}_1\hat{s}_2 + \hat{s}_1\hat{s}_3 + \hat{s}_2\hat{s}_3)$$

$$\widehat{H}_{dip}^{ij} = \frac{\mu_0}{4\pi r^3}\left[\vec{\boldsymbol{\mu}}_{\boldsymbol{i}} \cdot \vec{\boldsymbol{\mu}}_{\boldsymbol{j}} - \frac{3}{r}\left(\vec{\boldsymbol{\mu}}_{\boldsymbol{i}} \cdot \vec{\boldsymbol{r}}_{\boldsymbol{ij}}\right)\left(\vec{\boldsymbol{\mu}}_{\boldsymbol{j}} \cdot \vec{\boldsymbol{r}}_{\boldsymbol{ij}}\right)\right],$$

where $\vec{\boldsymbol{\mu}}_{\boldsymbol{i}}$ is the magnetic moment of site i, $\vec{\boldsymbol{r}}_{\boldsymbol{ij}}$ is the directional vector connecting the sites i and j, r is the distance between the two interacting sites, $\hat{s}_i$ is the ground state pseudospin on site i. The total dipolar Hamiltonian is a sum of $\widehat{H}_{dip}^{ij}$ for all interacting pairs ($i \neq j$). The total exchange Hamiltonian is expanded in the basis of products of local eigenstates (obtained *ab initio*) and is then diagonalized. The resulting exchange eigenstates are subsequently used to compute the magnetic properties of the entire Dy_3 unit, which can be directly compared to the measured molar magnetization and magnetic susceptibility. This approach relies on a single parameter *J* as the fitting parameter for each interacting pair; however, in this particular case, given the C_3 point group symmetry of the investigated **R/S-Dy3** compounds, all interactions have the same strength, $J_{12} = J_{13} = J_{23} = J$.

As an alternative, broken-symmetry DFT calculations[26-28] of magnetic exchange were done using the ORCA 6.1.0 package.[29-31] For these calculations, the same structural unit of the Dy_3 molecule was employed as for the multireference calculations with OpenMOLCAS: the distant bulky ligands were removed while the dangling bonds were saturated by H atoms. All Dy^{3+} were replaced by Gd^{3+}, to avoid failure of the DFT calculations due to near-degeneracy of the ground state of the Dy^{3+}. Three structural units were generated for each molecule: each structure contains two magnetic sites, while diamagnetic Lu^{3+} replaces the third metal site. Since the calculated magnetic exchange refers to the two interacting spins $S = 7/2$ for Gd^{3+}, they need to be rescaled up to reflect the true spin of the Dy^{3+} ($S = 5/2$): to this end, the scaling factor of 49/25 = 1.96 was applied to the values printed in the output files.

The B3LYP density functional was employed in all BS-DFT calculations.[32, 33]

In all non-relativistic calculations, all atoms were described by the def2-SVP and def2-TZVP basis sets.[33] Relativistic corrections were considered within the X2C method, as implemented in ORCA, which required using adapted basis sets: x2c-SVPall and x2c-TZVPall, respectively.[34] All calculations were sped up by the resolution of identity (RI) methods, where all auxiliary density fitting basis sets were generated on the fly using the "AutoAux" generation procedure, as implemented in ORCA.[35] Accurate density integration grids were employed, as defined by the DEFGRID3 keyword. An approximate second-order convergence method accelerated all DFT.[36]

The obtained results are gathered in Supplementary Tables 9-10. The obtained values of magnetic exchange in BS-DFT calculations are in reasonable agreement with the parameters of magnetic exchange obtained from the POLY_ANISO description of the magnetism.

Computational results:

Supplementary Table 6 *Ab initio* energy structure for the ground $J = 15/2$ multiplet of the Dy sites in **R-Dy$_3$** and **S-Dy$_3$** compounds.

S-Dy$_3$				**R-Dy$_3$**			
CASSCF/SO		**CASPT2/SO**		**CASSCF/SO**		**CASPT2/SO**	
Energy (cm^{-1})	Main values of the *g*-tensor	Energy (cm^{-1})	Main values of the *g*-tensor	Energy (cm^{-1})	Main values of the *g*-tensor	Energy (cm^{-1})	Main values of the *g*-tensor
0.0 0.0	0.4099 1.4363 17.0998	0.0 0.0	0.3652 1.1821 17.4515	0.0 0.0	0.2786 0.6872 18.4337	0.0 0.0	0.1937 0.5126 18.6806
25.6 25.6	0.1507 1.2795 15.1431	42.5 42.5	0.3149 1.2231 15.2765	35.5 35.5	0.1938 1.1190 17.2579	60.1 60.1	0.4109 1.1210 17.1793
59.0 59.0	0.3657 1.3377 15.1308	96.6 96.6	0.2399 1.3061 15.4149	70.6 70.6	0.3160 0.9811 16.4091	116.3 116.3	0.1488 1.1699 16.2645
110.3 110.3	0.7751 1.8801 14.3397	162.9 162.9	0.3860 1.6649 14.6865	115.5 115.5	1.3444 2.5555 14.7479	173.7 173.7	1.0152 2.5004 14.8967
146.2 146.2	5.6955 6.2638 8.6504	209.2 209.2	5.2094 6.5320 9.6617	150.9 150.9	5.0413 5.7972 9.1908	221.7 221.7	4.9375 5.6852 10.1847
208.9 208.9	0.2425 3.2250 15.4596	307.3 307.3	0.0445 2.9271 15.7544	209.3 209.3	0.5158 3.0913 16.0958	315.1 315.1	0.2540 2.7738 16.5255
236.6 236.6	0.8447 2.1770 17.0255	341.5 341.5	0.7574 2.1457 17.2124	234.6 234.6	0.7139 1.8786 16.9842	344.1 344.1	0.6053 1.8160 17.2843
381.3 381.3	0.0340 0.0534 19.4082	532.7 532.7	0.0410 0.0665 19.4631	388.8 388.8	0.0249 0.0408 19.4196	549.0 549.0	0.0262 0.0501 19.4785
Angle between the ground state main magnetic axis and the Dy_3 plane (degrees)							
	3.38		2.15		0.72		1.11

Supplementary Table 7 Crystal field parameters the ground $J = 15/2$ multiplet. The quantization axis is the g_Z axis of the ground Kramers doublet state.

Rank	Projection	**S-Dy$_3$**		**R-Dy$_3$**	
		CASSCF/SO	**CASPT2/SO**	**CASSCF/SO**	**CASPT2/SO**
2	-2	0.611920E+00	1.591636E+00	-0.938342E+00	-1.749693E+00
	-1	-0.232513E+01	6.557662E-01	0.310623E+01	1.839201E+00
	0	-0.999577E+00	9.211302E-01	-0.495616E+00	9.741963E-01
	+1	0.863028E+00	-2.486650E+00	0.688160E+00	1.404378E+00
	+2	-0.695278E-01	-1.350604E+00	0.113886E+00	-3.611147E-01
4	-4	-0.695737E-02	-4.887727E-03	0.165560E-02	-7.511037E-03
	-3	0.468768E-01	-9.436257E-03	-0.336538E-01	-6.718870E-03
	-2	0.947452E-02	3.537860E-02	-0.180756E-01	-1.362814E-03
	-1	0.278866E-01	-5.309757E-04	-0.191664E-01	2.778443E-02
	0	0.483624E-03	-3.838408E-03	-0.424155E-02	-3.851749E-03
	+1	0.781216E-02	-2.969632E-02	-0.727539E-02	1.380266E-02
	+2	0.666318E-02	1.997272E-02	-0.138493E-01	-4.229186E-02
	+3	0.839755E-01	1.935300E-02	0.402194E-01	2.660325E-02
	+4	0.115444E-03	1.162522E-02	-0.107180E-01	-1.215216E-02
6	-6	-0.204052E-04	5.287139E-05	0.254977E-03	3.757630E-05
	-5	0.515593E-03	9.793606E-04	-0.260451E-03	-2.974809E-04
	-4	0.687619E-04	2.287951E-04	0.136048E-03	2.242842E-05
	-3	-0.250856E-03	-3.336923E-04	-0.146387E-03	-3.428878E-04
	-2	0.532856E-05	3.123078E-04	-0.193868E-04	-1.499573E-04
	-1	-0.972141E-04	2.298824E-04	-0.160163E-03	-1.237670E-04
	0	0.125102E-05	1.083841E-05	-0.285801E-05	1.153015E-05
	+1	0.407949E-04	7.933309E-06	0.619403E-04	2.078112E-04
	+2	0.146681E-03	2.594679E-05	0.826131E-04	-2.890169E-04
	+3	-0.438927E-04	-5.693858E-05	-0.100462E-03	-1.244238E-05
	+4	0.139618E-03	-1.551434E-04	0.269905E-04	2.796015E-04
	+5	-0.110153E-02	2.653561E-04	-0.106421E-02	-9.478662E-04
	+6	-0.265204E-04	-2.848074E-05	0.505041E-04	-1.739805E-05

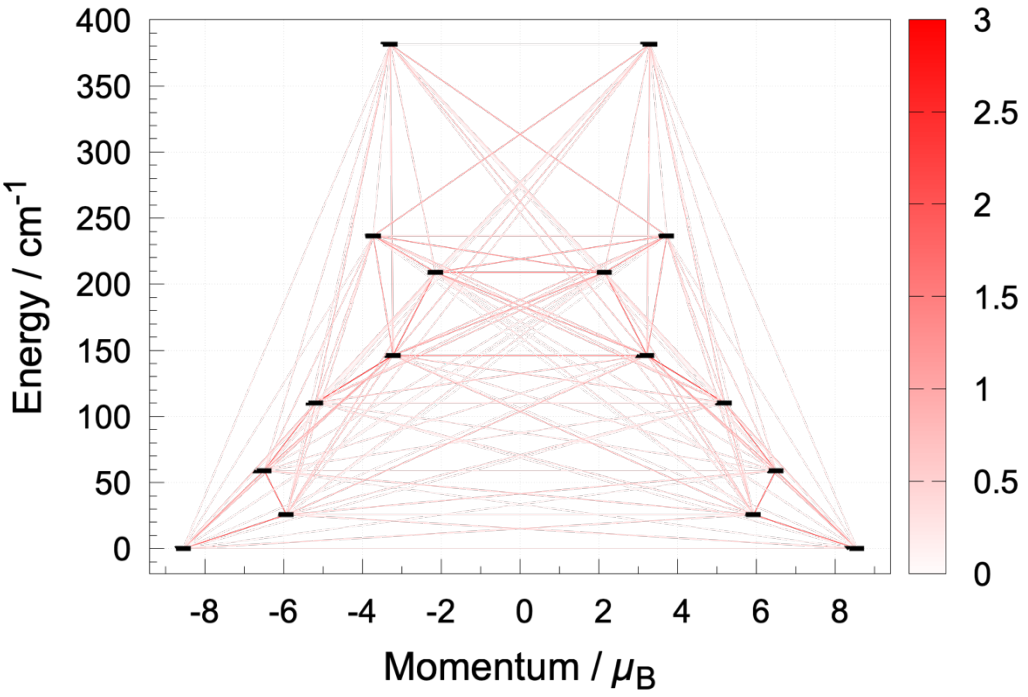

Supplementary Figure 40 Blocking barrier of one single Dy site in **S-Dy3**, using the CASSCF results.

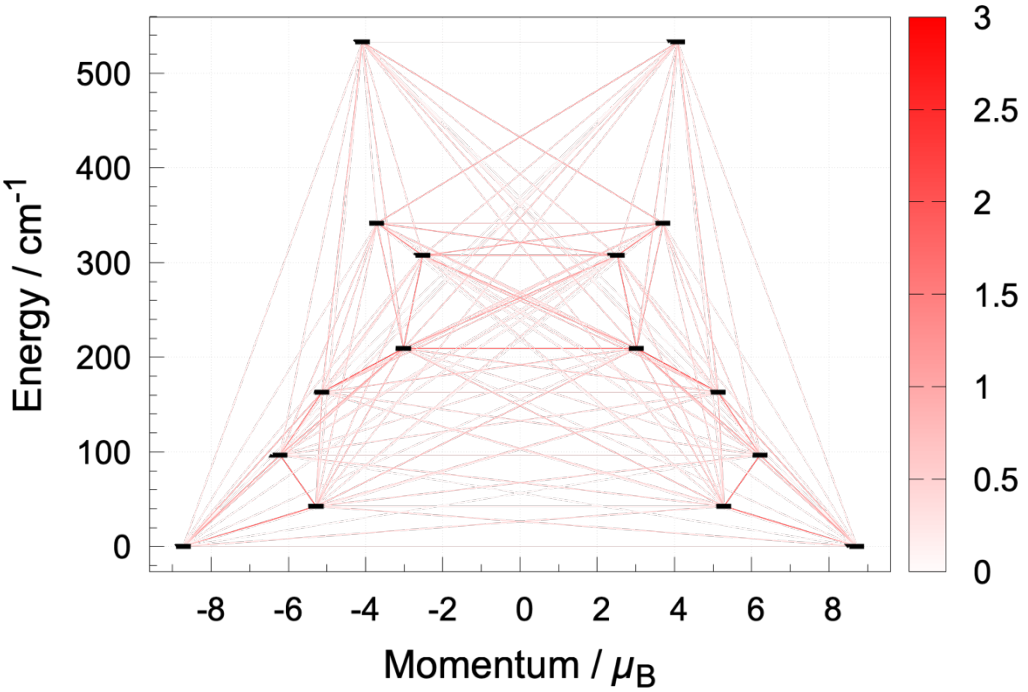

Supplementary Figure 41 Blocking barrier of one single Dy site in **S-Dy3**, using the CASPT2/SO results.

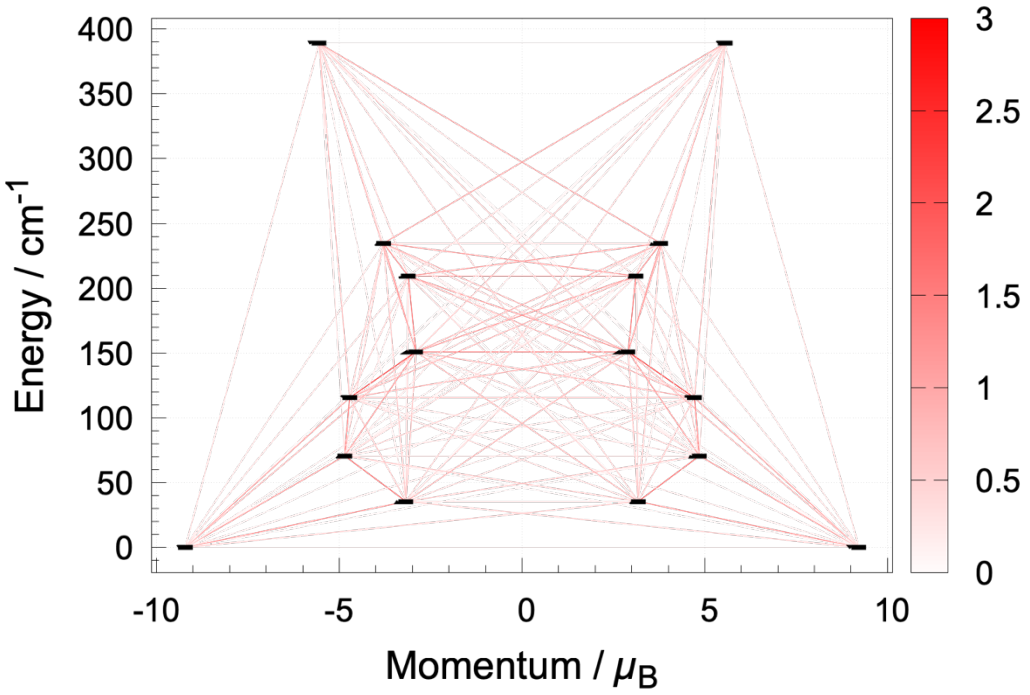

Supplementary Figure 42 Blocking barrier of one single Dy site in **R-Dy3**, using the CASSCF results.

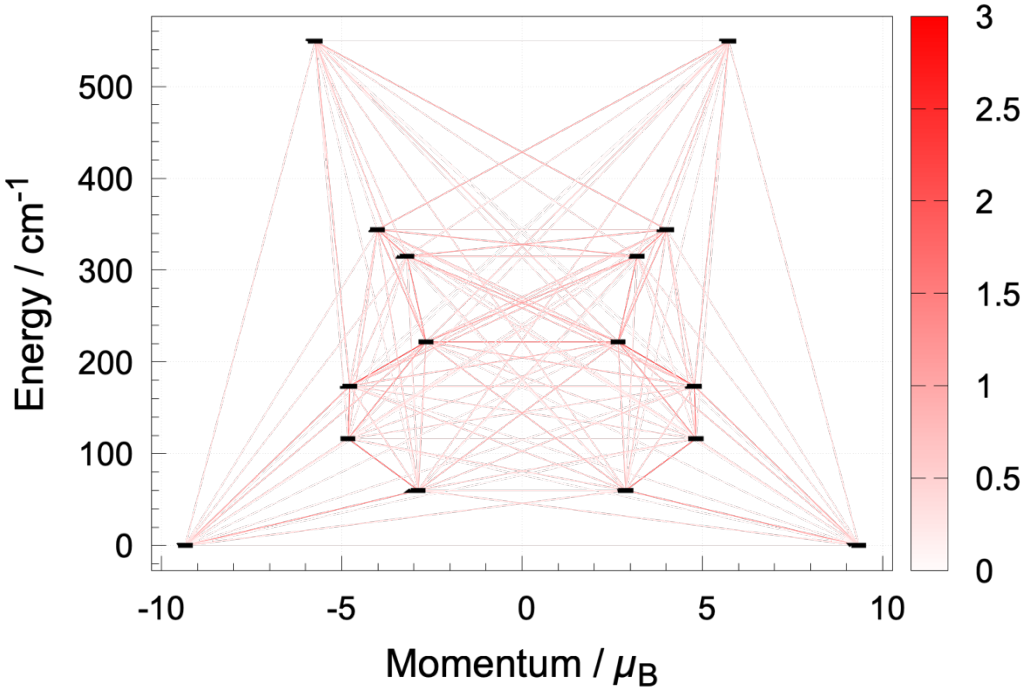

Supplementary Figure 43 Blocking barrier of one single Dy site in **R-Dy3**, using the CASSPT2/SO results.

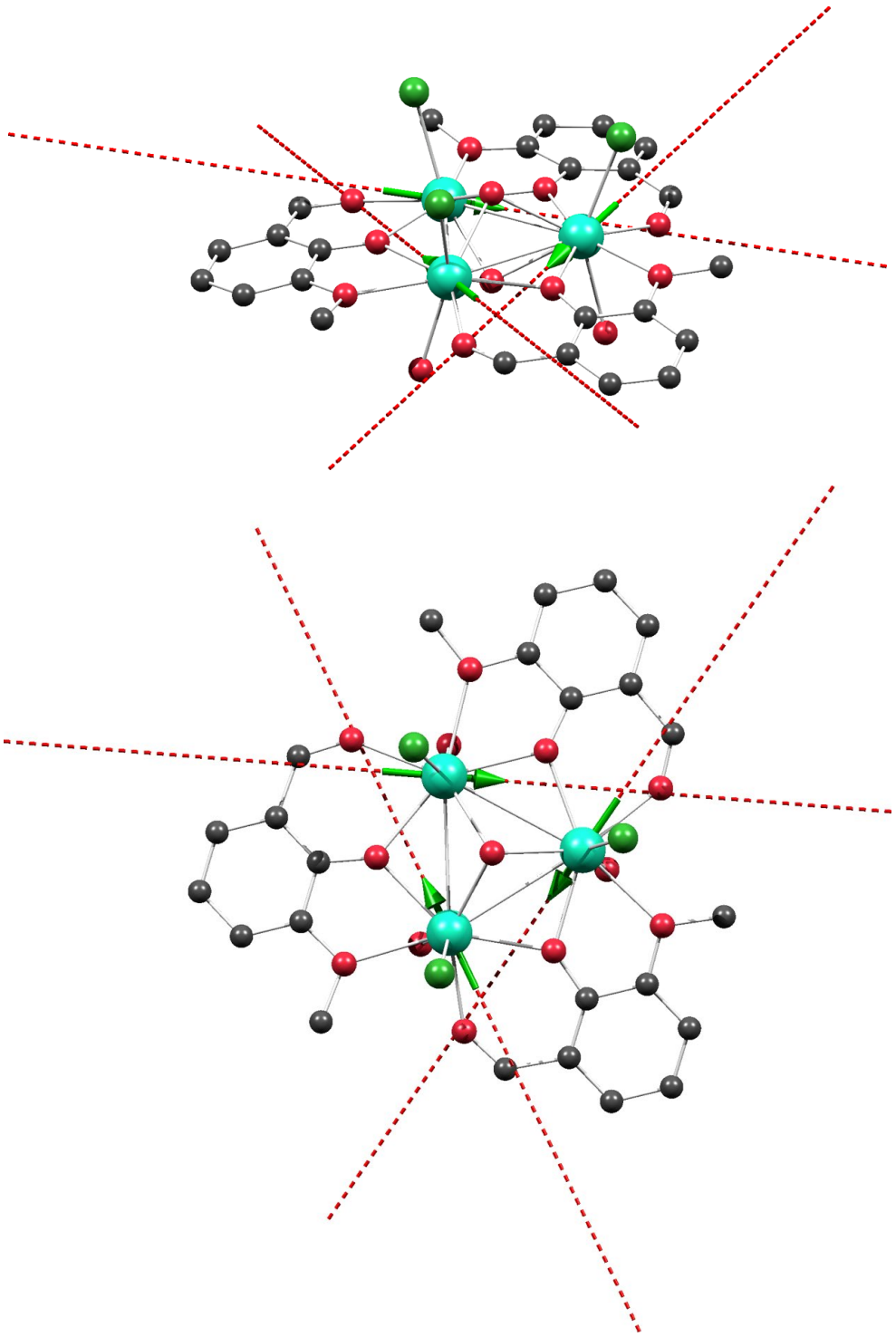

Supplementary Figure 44 Orientation of main magnetic axes in **S-Dy$_3$** with respect to the molecular frame.

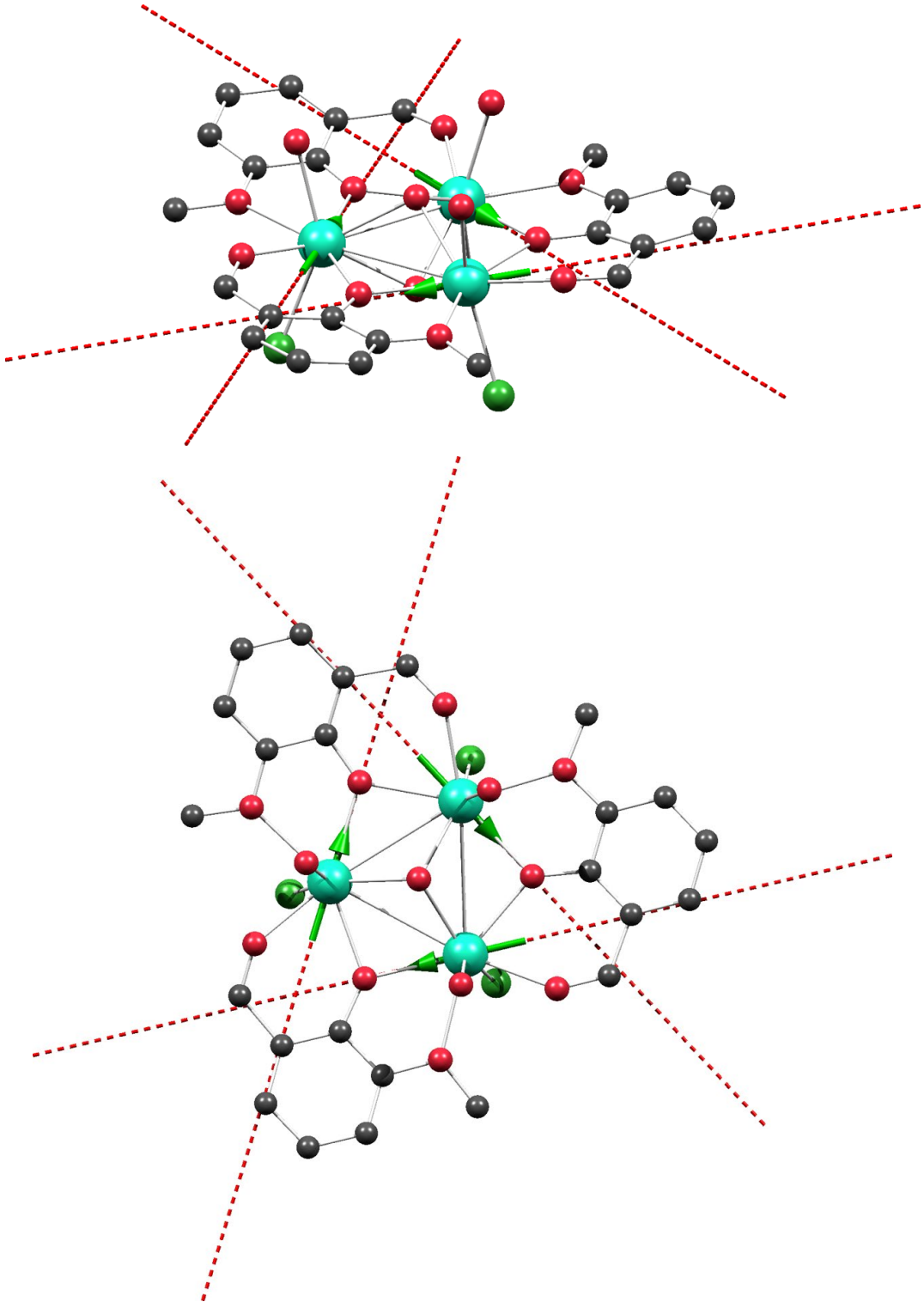

Supplementary Figure 45 Orientation of main magnetic axes in **R-Dy$_3$** with respect to the molecular frame.

Supplementary Table 8 Low-lying exchange energy spectra of the investigated Dy_3 compounds.

S-Dy_3		**R-Dy_3**	
CASSCF/SO	**CASPT2/SO**	**CASSCF/SO**	**CASPT2/SO**
J = -0.530 cm^{-1}	J = -0.405 cm^{-1}	J = -0.220 cm^{-1}	J = -0.220 cm^{-1}
0.000000	0.000000	0.000000	0.000000
0.000000	0.000000	0.000000	0.000000
4.679366	4.884280	5.411856	5.731996
4.679366	4.884280	5.411856	5.731996
5.089995	5.147786	5.477192	5.781325
5.089995	5.147786	5.477192	5.781325
5.401040	5.354439	5.525515	5.821571
5.401040	5.354439	5.525515	5.821571
27.064661	44.095682	37.640382	62.318454
27.064661	44.095682	37.640382	62.318454
27.399789	44.321227	37.676270	62.354481
27.399789	44.321227	37.676270	62.354481
27.770585	44.687782	37.815855	62.522991
27.770585	44.687782	37.815855	62.522991
28.978735	45.847305	38.829480	63.646681
28.978735	45.847305	38.829480	63.646681
28.984377	45.865443	38.832669	63.649443
28.984377	45.865443	38.832669	63.649443
29.065111	45.900542	38.842457	63.659252
29.065111	45.900542	38.842457	63.659252
…	…	…	…
g-tensor of the ground exchange doublet state			
0.0000	0.0000	0.0000	0.0000
0.0000	0.0000	0.0000	0.0000
4.6028	2.4933	3.4223	1.6707

In all the cases, the main exchange axis g_Z of the ground doublet state points perpendicularly to the plane of the Dy_3 triangle.

Supplementary Table 9 BS-DFT exchange parameters (in cm^{-1}) for **S-Dy$_3$** compound.

Basis	Energy HS	$\langle S^2 \rangle$ for HS	Energy BS	$\langle S^2 \rangle$ for BS	*J*(1)	*J*(2)	*J*(3)
Def2-SVP	-6130.326524	56.4779	-6130.326615	7.4765	-0.80	-0.71	-0.80
Def2-TZVP	-6133.143337	56.4790	-6133.143434	7.4776	-0.84	-0.74	-0.84
x2c-SVPall	-40474.719183	56.0119	-40474.719214	7.0118	-0.27	-0.24	-0.27
x2c-TZVPall	-40479.119701	56.0126	-40479.119733	7.0125	-0.27	-0.24	-0.27

Supplementary Table 10 BS-DFT exchange parameters (in cm^{-1}) for **R-Dy$_3$** compound.

Basis	Energy HS	$\langle S^2 \rangle$ for HS	Energy BS	$\langle S^2 \rangle$ for BS	*J*(1)	*J*(2)	*J*(3)
Def2-SVP	-6130.365039	56.4747	-6130.365149	7.4730	-0.96	-0.84	-0.96
Def2-TZVP	-6133.176352	56.4761	-6133.176471	7.4743	-1.04	-0.92	-1.04
x2c-SVPall	-40474.758687	56.0118	-40474.758718	7.0118	-0.27	-0.24	-0.27
x2c-TZVPall	-40479.153349	56.0126	-40479.153381	7.0125	-0.27	-0.25	-0.27

- *J*(1) formula, as reported in a) A.P. Ginsberg *J. Am. Chem. Soc.* 102 (1980), 111; b) L. Noodleman *J. Chem. Phys.* 74 (1981), 5737; c) L. Noodleman, E.R. Davidson *Chem. Phys.* 109 (1986), 131.
- *J*(2) formula, as reported in A. Bencini, D. Gatteschi *J. Am. Chem. Soc.* 108 (1980), 5763.
- *J*(3) formula, as reported in a) K. Yamaguchi, Y. Takahara, T. Fueno in: V. H. Smith (Ed.) Applied Quantum Chemistry. Reidel, Dordrecht (1986), pp 155.; b) T. Soda et al. *Chem. Phys. Lett.* 319, (2000), 223.

Simulation of the magnetism in the entire unit cell of S-Dy_3 and R-Dy_3 compounds

For this study, two approaches were undertaken.
1) The POLY_ANISO code was updated to include the periodicity into account. This part took most of the time and is still under verification/validation. These results are not discussed here.
2) All four molecules in the unit cell were computed by *ab initio* calculations (12 sites), making the results below possible.

The four molecules have been placed at their exact position in the unit cell, keeping their orientation. The intra-molecular magnetic exchange was kept identical to the one obtained above. The intra-molecular dipole-dipole interactions were considered.
Only the ground Kramers doublet from each Dy site was kept as the local basis in these simulations, which gives rise to $2^{12} = 4096$ coupled functions.

The low-lying energy spectra combine toroidal moments arising from each Dy_3 molecule in the unit cell. Since the toroidal moment of each molecule can take 2 directions (+, -) there are $2^4 = 16$ low-lying energy states in the ground term. These states are plotted separately, and the relative orientations of the local toroidal moments are analyzed.

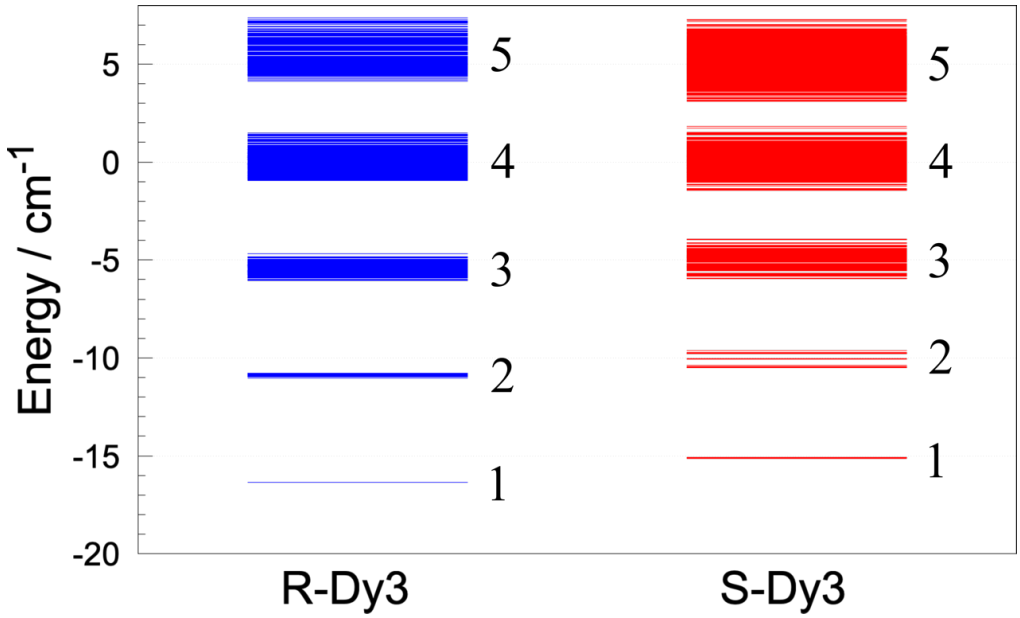

Supplementary Figure 46 The full exchange energy spectrum (4096 exchange levels) for **R-Dy_3** and **S-Dy_3**. The numbers 1-5 indicate the group number (See Supplementary Table 11 for details).

Supplementary Table 11 explains the spectrum of the four Dy_3 molecules in the unit cell, as depicted above. The low-lying energy spectrum of a single Dy_3 triangle comprises eight coupled states: the lowest two states have a large toroidal moment ($\tau_z = \pm 60\ \mu_B$Å), while the other six states are excited states, and represent the reversal of one magnetic moment of a single metal site, with toroidal moment value of ($\tau_z = \pm 20\ \mu_B$Å). Let's denote the states on the molecule i with a large toroidal moment by $|L_i\rangle$, while the six states with small toroidal moment – by $|s_i\rangle$.

Supplementary Table 11 Description of the nature of the coupled states of the four Dy_3 molecules in the unit cell.

Group	Number of states in group	State numbers (min-max)	Coupled states	Description
1	16 ($=2^4$)	1-16	$\|L_1L_2L_3L_4\rangle$	All four molecules are in their ground state, with large toroidal moments
2	192 ($=4\times2^3\times6$)	17-208	$\|s_1L_2L_3L_4\rangle$ $\|L_1s_2L_3L_4\rangle$ $\|L_1L_2s_3L_4\rangle$ $\|L_1L_2L_3s_4\rangle$	One of the four molecules has one of the local moments reversed, and a small toroidal moment it. The other three molecule are in their ground states, with large toroidal moments.
3	864 ($=6\times2^2\times6^2$)	209-1072	$\|s_1s_2L_3L_4\rangle$ $\|s_1L_2s_3L_4\rangle$ $\|s_1L_2L_3s_4\rangle$ $\|L_1s_2s_3L_4\rangle$ $\|L_1s_2L_3s_4\rangle$ $\|L_1L_2s_3s_4\rangle$	Two of the four molecules have one of the local moments reversed, and a small toroidal moment. The other two molecule are in their ground states, with large toroidal moments.
4	1728 ($=4\times2\times6^3$)	1073-2800	$\|s_1s_2s_3L_4\rangle$ $\|s_1s_2L_3s_4\rangle$ $\|s_1L_2s_3s_4\rangle$ $\|L_1s_2s_3s_4\rangle$	Three of the four molecules have one of the local moments reversed, and a small toroidal moment. One molecule of the four is in its ground state, with large toroidal moment.
5	1296 ($=6^4$)	2801-4096	$\|s_1s_2s_3s_4\rangle$	All four molecules have one of the local moments reversed, and a small toroidal moment

Supplementary Table 12 Low-lying exchange energy spectra of the investigated **R-Dy$_3$** compounds, alongside with the local orientation of the molecular toroidal moment. In this table, the "+" means that the toroidal moment of the respective triangle is oriented towards water ligands, while "-" means that the toroidal moment is oriented in the opposite direction, towards Cl ligands.

	Absolute Exchange energies in cm^{-1}	Relative Exchange energies in cm^{-1}	Toroidal moment on individual molecules in the unit cell			
			Mol. 1	Mol. 2	Mol. 3	Mol. 4
1	-16.355495138	0.000000000	-	-	-	-
2	-16.355495136	0.000000000	+	+	+	+
3	-16.355347563	0.000147574	-	-	+	-
4	-16.355347560	0.000147577	+	-	-	-
5	-16.355347552	0.000147585	+	+	-	+
6	-16.355347552	0.000147585	-	+	+	+
7	-16.355347515	0.000147623	-	+	-	-
8	-16.355347514	0.000147624	+	-	+	+
9	-16.352955475	0.002539662	+	+	-	-
10	-16.352955474	0.002539664	-	-	+	+
11	-16.352955425	0.002539713	+	-	+	-
12	-16.352955422	0.002539716	-	+	-	+
13	-16.352955264	0.002539874	-	+	+	-
14	-16.352955262	0.002539875	+	-	-	+
15	-16.348318530	0.007176607	+	+	+	-
16	-16.348318529	0.007176608	-	-	-	+
…	…	…	…	…	…	…

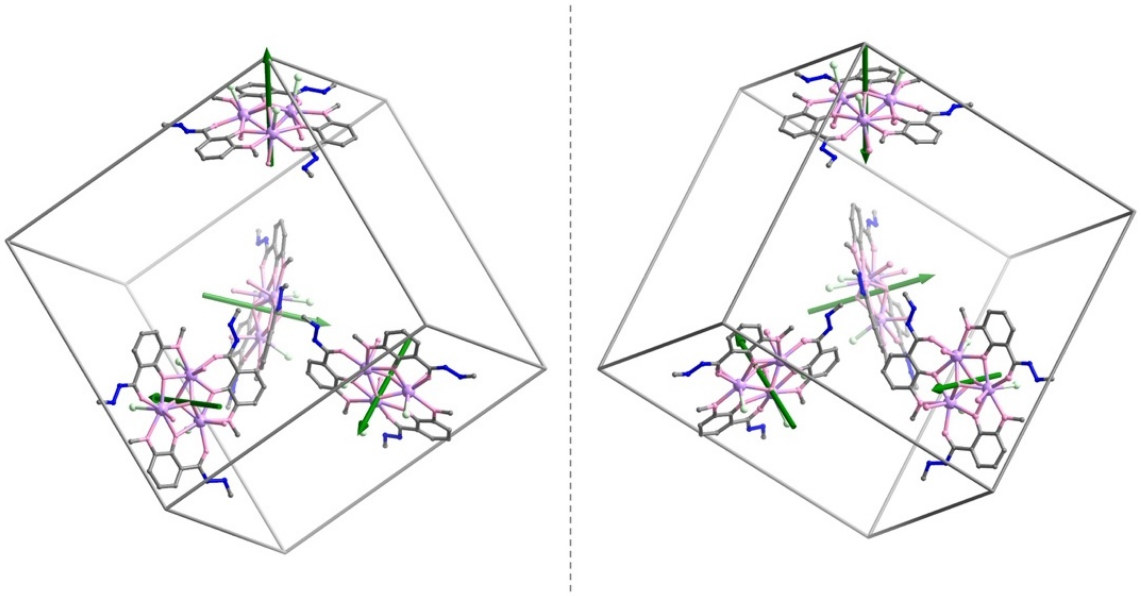

Supplementary Figure 47 The directions of toroidal moments of four molecules (green arrows) in the unit cell for **R-Dy$_3$** (left) and **S-Dy$_3$** (right) obtained from *ab initio* calculations.

Supplementary Table 13 Low-lying exchange energy spectra of the investigated **S-Dy$_3$** compounds, alongside the local orientation of the molecular toroidal moment. In this table, the "+" means that the toroidal moment of the respective triangle is oriented towards water ligands, while "-" means that the toroidal moment is oriented in the opposite direction, towards Cl ligands.

	Absolute Exchange energies in cm^{-1}	Relative Exchange energies in cm^{-1}	Toroidal moment on individual molecules in the unit cell			
			Mol. 1	Mol. 2	Mol. 3	Mol. 4
1	-15.129766257	0.000000000	+	+	+	+
2	-15.129766256	0.000000000	-	-	-	-
3	-15.101060496	0.028705761	+	+	+	-
4	-15.101060493	0.028705763	-	-	-	+
5	-15.097586532	0.032179725	-	-	+	-
6	-15.097586526	0.032179731	+	+	-	+
7	-15.097586498	0.032179759	-	+	-	-
8	-15.097586489	0.032179768	+	-	+	+
9	-15.097586145	0.032180112	+	-	-	-
10	-15.097586140	0.032180116	-	+	+	+
11	-15.088017694	0.041748563	+	+	-	-
12	-15.088017684	0.041748573	-	-	+	+
13	-15.088017323	0.041748933	-	+	+	-
14	-15.088017321	0.041748936	+	-	-	+
15	-15.088016545	0.041749712	+	-	+	-
16	-15.088016527	0.041749729	-	+	-	+
…	…	…	…	…	…	…

Derivation of the toroidal moment for a Dy_3 triangle, regular triangle, pure Ising spin

As shown in Supplementary Figure 45, three metal sites are positioned at the vertices of an equilateral triangle ABC with side length L ($AB = BC = CA = L$). The triangle is centered at the origin of the coordinate system, with each vertex located at a distance $r = OA = OB = OC = \frac{L}{\sqrt{3}}$ from the center. Each local site possesses a uniaxial magnetic moment along its own direction.

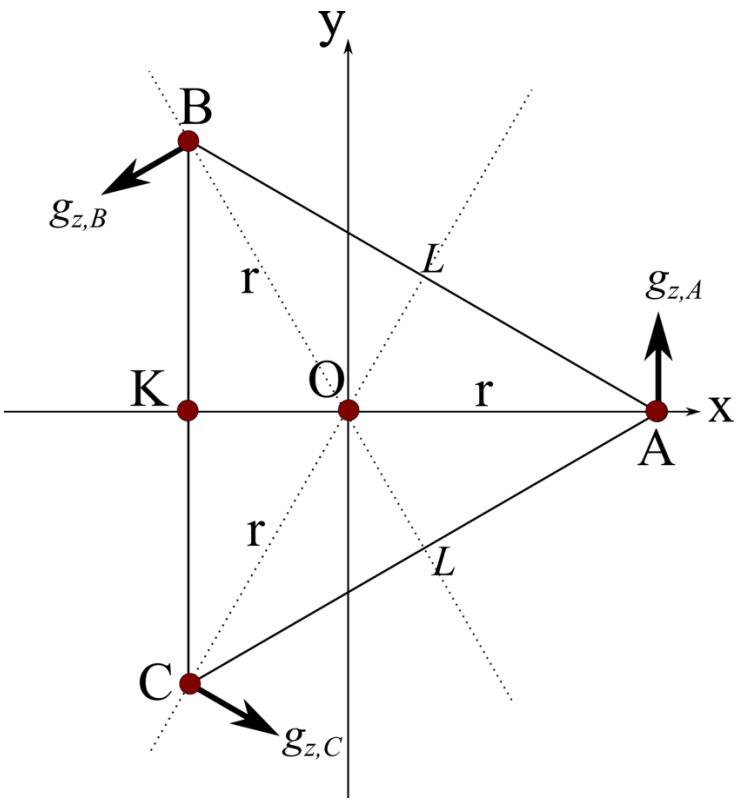

Supplementary Figure 48 The model setup for the evaluation of the toroidal moment for the anticlockwise magnetic configuration.

Coordinates of the metal sites:

Metal site	in term of L			in terms of $r = \frac{L}{\sqrt{3}}$		
	x	**y**	**z**	**x**	**y**	**z**
A, $\vec{r}_A$	$\frac{L}{\sqrt{3}}$	0	0	r	0	0
B, $\vec{r}_B$	$-\frac{L}{2\sqrt{3}}$	$\frac{L}{2}$	0	$-\frac{r}{2}$	$\frac{r\sqrt{3}}{2}$	0
C, $\vec{r}_C$	$-\frac{L}{2\sqrt{3}}$	$-\frac{L}{2}$	0	$-\frac{r}{2}$	$-\frac{r\sqrt{3}}{2}$	0

Due to the dipole-dipole and magnetic exchange interactions among the local magnetic moments, the ground state of the Dy_3 triangle exhibits a doubly degenerate toroidal configuration, with clockwise and counterclockwise arrangements of the moments.

In the following analysis, we focus on the counterclockwise toroidal arrangement. The local magnetic moments are treated as Ising-like and uniaxial, with non-zero components only along their local easy axes (g_z). All moments are assumed to have identical magnitudes, given in units of Bohr magnetons (μ_B) as: $\vec{\mu}_A = \vec{\mu}_B = \vec{\mu}_C = \frac{g_z}{2}$

In the general coordinate system defined above, the local magnetic moment vectors are expressed as:

Local magnetic moments in the general coordinate system:

Metal site	Anticlockwise arrangement			Clockwise arrangement		
	x	**y**	**z**	**x**	**y**	**z**
$\vec{\mu}_A$	0	$\frac{g_z}{2}$	0	0	$-\frac{g_z}{2}$	0
$\vec{\mu}_B$	$-\frac{g_z\sqrt{3}}{4}$	$-\frac{g_z}{4}$	0	$\frac{g_z\sqrt{3}}{4}$	$\frac{g_z}{4}$	0
$\vec{\mu}_C$	$\frac{g_z\sqrt{3}}{4}$	$-\frac{g_z}{4}$	0	$-\frac{g_z\sqrt{3}}{4}$	$\frac{g_z}{4}$	0

Check the length of the local moment:

$$|\vec{\mu}_A| = \sqrt{\left(\frac{g_z}{2}\right)^2} = \frac{g_z}{2}$$

$$|\vec{\mu}_B| = \sqrt{\left(-\frac{g_z\sqrt{3}}{4}\right)^2 + \left(-\frac{g_z}{4}\right)^2} = \sqrt{\frac{3}{16}(g_z)^2 + \frac{1}{16}(g_z)^2} = \sqrt{\frac{4}{16}(g_z)^2} = \frac{g_z}{2}$$

$$|\vec{\mu}_C| = \sqrt{\left(\frac{g_z\sqrt{3}}{4}\right)^2 + \left(-\frac{g_z}{4}\right)^2} = \sqrt{\frac{3}{16}(g_z)^2 + \frac{1}{16}(g_z)^2} = \sqrt{\frac{4}{16}(g_z)^2} = \frac{g_z}{2}$$

The toroidal moment is calculated as:

$$\tau = \sum_i^3 \vec{r}_i \times \vec{\mu}_i = (\vec{r}_A \times \vec{\mu}_A) + (\vec{r}_B \times \vec{\mu}_B) + (\vec{r}_C \times \vec{\mu}_C)$$

The cross-product formula is:

$$\vec{r}_i \times \vec{\mu}_i = \begin{vmatrix} \mathbf{i} & \mathbf{j} & \mathbf{k} \\ r_{i,x} & r_{i,y} & r_{i,z} \\ \mu_{i,x} & \mu_{i,y} & \mu_{i,z} \end{vmatrix} = \left(r_{i,y}\mu_{i,z} - r_{i,z}\mu_{i,y}\right)\mathbf{i} + \left(-r_{i,x}\mu_{i,z} + r_{i,z}\mu_{i,x}\right)\mathbf{j} + \left(r_{i,x}\mu_{i,y} - r_{i,y}\mu_{i,x}\right)\mathbf{k}$$

Where $\mathbf{i}, \mathbf{j}, \mathbf{k}$ are unit vectors along the Cartesian axes, x, y, and z, respectively.

For site A, we have:

$$\vec{r}_A \times \vec{\mu}_A = (r_{A,y}\mu_{A,z} - r_{A,z}\mu_{A,y})\mathbf{i} + (-r_{A,x}\mu_{A,z} + r_{A,z}\mu_{A,x})\mathbf{j} + (r_{A,x}\mu_{A,y} - r_{A,y}\mu_{A,x})\mathbf{k}$$

$$= \left(0 \cdot 0 - 0 \cdot \frac{g_z}{2}\right)\mathbf{i} + \left(-\frac{L}{\sqrt{3}} \cdot 0 + 0 \cdot 0\right)\mathbf{j} + \left(\frac{L}{\sqrt{3}} \cdot \frac{g_z}{2} - 0 \cdot 0\right)\mathbf{k} = \frac{Lg_z}{2\sqrt{3}}\mathbf{k}$$

For site B, we have:

$$\vec{r}_B \times \vec{\mu}_B = (r_{B,y}\mu_{B,z} - r_{B,z}\mu_{B,y})\mathbf{i} + (-r_{B,x}\mu_{B,z} + r_{B,z}\mu_{B,x})\mathbf{j} + (r_{B,x}\mu_{B,y} - r_{B,y}\mu_{B,x})\mathbf{k}$$

$$= \left(\frac{L}{2\sqrt{3}} \cdot 0 - 0 \cdot \left(-\frac{g_z}{4}\right)\right)\mathbf{i} + \left(\frac{L}{2} \cdot 0 + 0 \cdot \left(-\frac{g_z\sqrt{3}}{4}\right)\right)\mathbf{j}$$

$$+ \left(\left(-\frac{L}{2\sqrt{3}}\right) \cdot \left(-\frac{g_z}{4}\right) - \left(\frac{L}{2}\right) \cdot \left(-\frac{g_z\sqrt{3}}{4}\right)\right)\mathbf{k} = \left(\frac{Lg_z}{8\sqrt{3}} + \frac{Lg_z\sqrt{3}}{8}\right)\mathbf{k}$$

$$= \frac{Lg_z}{8}\left(\frac{1}{\sqrt{3}} + \sqrt{3}\right)\mathbf{k} = \frac{Lg_z}{8}\frac{4}{\sqrt{3}}\mathbf{k} = \frac{Lg_z}{2\sqrt{3}}\mathbf{k}$$

For site C, we have:

$$(\vec{r}_C \times \vec{\mu}_C) = (r_{C,y}\mu_{C,z} - r_{C,z}\mu_{C,y})\mathbf{i} + (-r_{C,x}\mu_{C,z} + r_{C,z}\mu_{C,x})\mathbf{j} + (r_{C,x}\mu_{C,y} - r_{C,y}\mu_{C,x})\mathbf{k}$$

$$= \left(\left(-\frac{L}{2\sqrt{3}}\right) \cdot 0 - 0 \cdot \left(-\frac{g_z}{4}\right)\right)\mathbf{i} + \left(\frac{L}{2} \cdot 0 + 0 \cdot \frac{g_z\sqrt{3}}{4}\right)\mathbf{j} + \left(\frac{L}{2\sqrt{3}} \cdot \frac{g_z}{4} + \frac{L}{2} \cdot \frac{g_z\sqrt{3}}{4}\right)\mathbf{k}$$

$$= \frac{Lg_z}{8}\left(\frac{1}{\sqrt{3}} + \sqrt{3}\right)\mathbf{k} = \frac{Lg_z}{2\sqrt{3}}\mathbf{k}$$

Note that the contributions of individual sites are identical. All contributions point in the same direction of the Cartesian axis z, as expected for an equilateral triangle.

$$\tau = \sum_i^3 \vec{r}_i \times \vec{\mu}_i = (\vec{r}_A \times \vec{\mu}_A) + (\vec{r}_B \times \vec{\mu}_B) + (\vec{r}_C \times \vec{\mu}_C) = \frac{Lg_z}{2\sqrt{3}}\mathbf{k} + \frac{Lg_z}{2\sqrt{3}}\mathbf{k} + \frac{Lg_z}{2\sqrt{3}}\mathbf{k} = \frac{Lg_z\sqrt{3}}{2}\mathbf{k}$$

For the case of the Dy_3 triangle, for the anticlockwise toroidal magnetic state, we have:
$r = 2.0$ Å and $g_z = 20\ \mu_B$, $L = r\sqrt{3}$, gives:

$$\tau = \frac{Lg_z\sqrt{3}}{2}\mathbf{k} = \frac{r\sqrt{3}\ g_z\sqrt{3}}{2}\mathbf{k} = \frac{3rg_z}{2}\mathbf{k} = \frac{3 \times 2.0\ \text{Å} \times 20\mu_B}{2}\mathbf{k} = 60\ \mu_B\text{Å}$$

Aligned along the cartesian axis z.

Note that the toroidal moment changes sign for the time-reversed state with clockwise arrangements of the local moments. This is a direct consequence of the change of sign of each local moment, see the table above.

The first excited state of the Dy_3 triangle corresponds to a reversal of one of the magnetic moments. This energy state is six-fold degenerate.

Consider the magnetic configuration where the local moment of site A is reversed compared to Figure 1. In such case, the toroidal moment is:

$$\begin{aligned}\vec{r}_A \times \vec{\mu}_A &= (r_{A,y}\mu_{A,z} - r_{A,z}\mu_{A,y})\mathbf{i} + (-r_{A,x}\mu_{A,z} + r_{A,z}\mu_{A,x})\mathbf{j} + (r_{A,x}\mu_{A,y} - r_{A,y}\mu_{A,x})\mathbf{k} \\ &= \left(0 \cdot 0 - 0 \cdot \left(-\frac{g_z}{2}\right)\right)\mathbf{i} + \left(-\frac{L}{\sqrt{3}} \cdot 0 + 0 \cdot 0\right)\mathbf{j} + \left(\frac{L}{\sqrt{3}} \cdot \left(-\frac{g_z}{2}\right) - 0 \cdot 0\right)\mathbf{k} \\ &= -\frac{Lg_z}{2\sqrt{3}}\mathbf{k}\end{aligned}$$

The total value of the toroidal moment is a sum of all contributions of all sites:

$$\tau = \sum_i^3 \vec{r}_i \times \vec{\mu}_i = (\vec{r}_A \times \vec{\mu}_A) + (\vec{r}_B \times \vec{\mu}_B) + (\vec{r}_C \times \vec{\mu}_C) = -\frac{Lg_z}{2\sqrt{3}}\mathbf{k} + \frac{Lg_z}{2\sqrt{3}}\mathbf{k} + \frac{Lg_z}{2\sqrt{3}}\mathbf{k} = \frac{Lg_z}{2\sqrt{3}}\mathbf{k}$$

Numerically, we have:

$$\tau = \frac{Lg_z}{2\sqrt{3}}\mathbf{k} = \frac{r\sqrt{3}\,g_z}{2\sqrt{3}}\mathbf{k} = \frac{rg_z}{2}\mathbf{k} = \frac{2.0\ \text{Å} \times 20\ \mu_B}{2} \approx 20\ \mu_B\text{Å}$$

From the output of Poly_Aniso:

Exchange state	Group Nr.	TOROIDAL MOMENT (in units of mu_Bohr * Angstrom) X	Y	Z	Norm
1	1	0.00000002	-0.00000001	60.03478956	60.03479
2	1	-0.00000002	0.00000001	-60.03478956	60.03479
3	1	0.00000001	0.00000003	-20.01159652	20.01160
4	1	0.00000001	-0.00000001	20.01159652	20.01160
5	1	0.00000002	0.00000002	20.01159652	20.01160
6	1	-0.00000002	-0.00000003	-20.01159652	20.01160
7	1	-0.00000001	0.00000001	-20.01159652	20.01160
8	1	-0.00000001	-0.00000003	20.01159652	20.01160

5. MChD measurements and spectroscopic analyses

MChD spectra were acquired on oriented single crystals of **R-Dy$_3$** and **S-Dy$_3$** (see main text for details). The samples were mounted on a titanium sample holder over a 0.9 mm hole diameter centered with respect to a 1.0 mm diameter collimated beam. Measurements were performed in the 2.2−50 K range with an alternating magnetic field $\boldsymbol{B}$ = ±0.5 T and ±1.0 T and frequency Ω = 0.04 Hz. MChD spectra as a function of the magnetic field were recorded at T = 2.2 K, 4.0 K and 7.0 K for alternating magnetic fields of different amplitudes (0.0-2.0 T). Unpolarized light was provided by a broadband Energetiq – Hamamatsu Laser Driven Light Sources (EQ-99X-FC-S or EQ-77X-FC-S). MChD spectra were obtained at each temperature/magnetic field value by collecting, on average, 50.000 spectra, with an integration time of 50 ms. The spectra were collected with a high resolution/high sensitivity Optosky detector equipped with a thermoelectric cooled sensor operating in the 200−1000 nm spectral region with an analogic/digital convertor of 16 bits. Each spectrum was correlated to a specific magnetic field value by a dual channel digitizer (Picoscope 5000B) acquiring simultaneously triggers from the spectrometer and the magnetic field from a calibrated Hall effect sensor (Lakeshore) placed in proximity of the sample. Data were then post-processed as a synchronous detection with a specific MatLab routine to obtain the MChD spectra. ΔA_{MChD} values were corrected by the sample thickness and concentration.

The MChD dissymmetry factor g_{MChD} is defined as follows:

$$g_{MChD} = \frac{\Delta A_{MChD}}{A\,\boldsymbol{B}} = \frac{(A(\boldsymbol{B}\uparrow\uparrow\boldsymbol{k}) - (A(\boldsymbol{B}\downarrow\uparrow\boldsymbol{k}))}{A\,\boldsymbol{B}} \qquad \text{(Equation 1)}$$

where ΔA_{MChD} is the differential absorption coefficient between the light absorption collected under a magnetic field parallel and antiparallel oriented with respect to the light wavevector $\boldsymbol{k}$, A is the effective absorption coefficients of the electronic transitions at zero field and $\boldsymbol{B}$ is the applied magnetic field intensity.

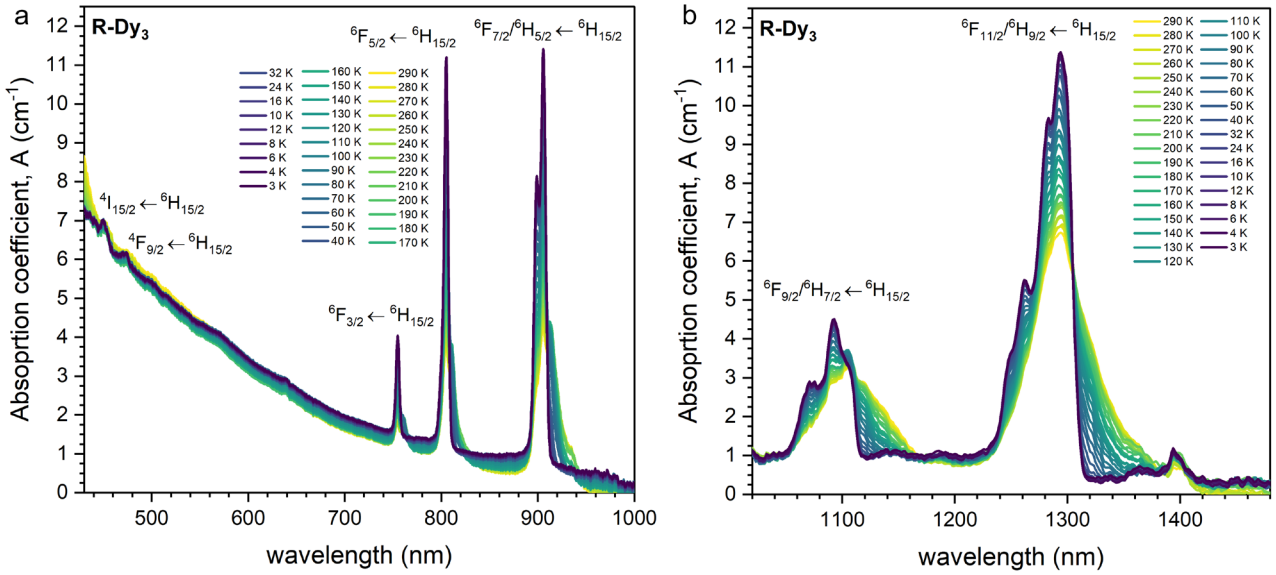

Supplementary Figure 49 Thermal variation (see legend) of the absorption coefficient for a single crystal of **R-Dy3** (***k*** ⊥ (111)) in the 430−1000 nm (a) and 1020−1480 nm (b) ranges. The spectroscopic terms of the *f-f* electronic transitions are indicated.

Supplementary Table 14 Assignment of the Dy(III) absorption peaks and $|g_{MChD}|$ values (T = 3.0 K, $\boldsymbol{B}$ = 1.0 T).

λ (nm)	***f-f* transition assignment**	**$\lvert g_{MChD}\rvert$ (T^{-1}), λ (nm)**
450	$^4I_{15/2} \leftarrow {}^6H_{15/2}$	0.03(1), 454.5 nm
475	$^4F_{9/2} \leftarrow {}^6H_{15/2}$	0.005(1), 473.6 nm
755	$^6F_{3/2} \leftarrow {}^6H_{15/2}$	0.001(1), 755.2 nm
806	$^6F_{5/2} \leftarrow {}^6H_{15/2}$	0.001(1), 803.2 nm
880-920	$^6F_{7/2}/{}^6H_{5/2} \leftarrow {}^6H_{15/2}$	0.003(1), 905.1 nm
1050-1120	$^6F_{9/2}/{}^6H_{7/2} \leftarrow {}^6H_{15/2}$	0.003(1), 1094.6 nm
1220-1320	$^6F_{11/2}/{}^6H_{9/2} \leftarrow {}^6H_{15/2}$	0.003(1), 1303.3 nm

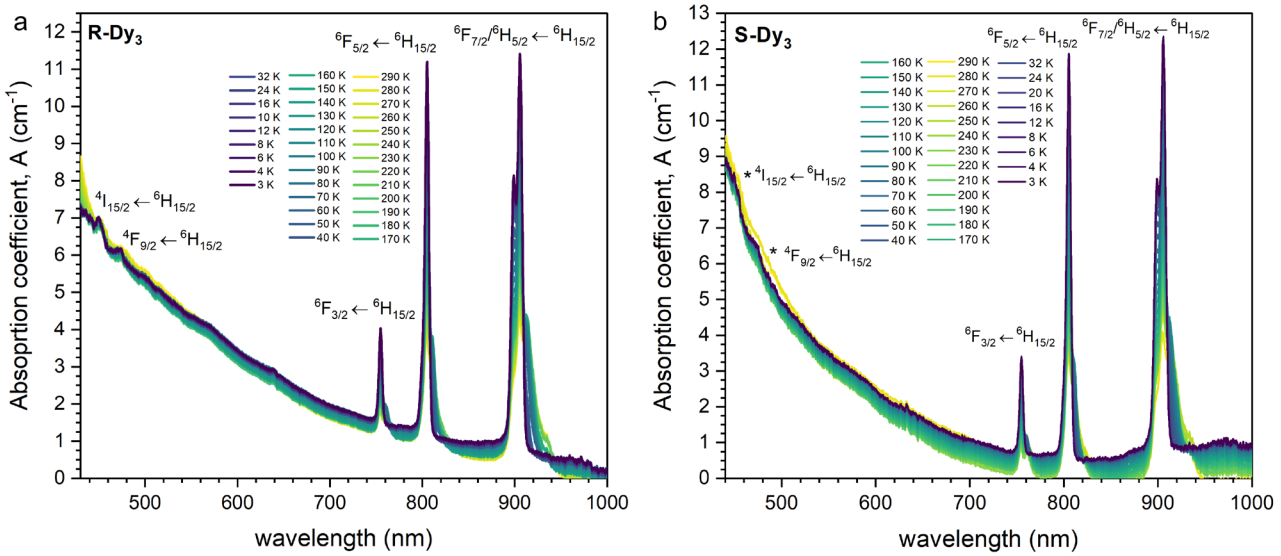

Supplementary Figure 50 Comparison of the thermal variation (see legend) of the absorption coefficient for single crystals of **R-Dy$_3$** and **S-Dy$_3$** (***k*** ⊥ (111)) in the 430−1000 nm range. The spectroscopic terms of the *f-f* electronic transitions are indicated.

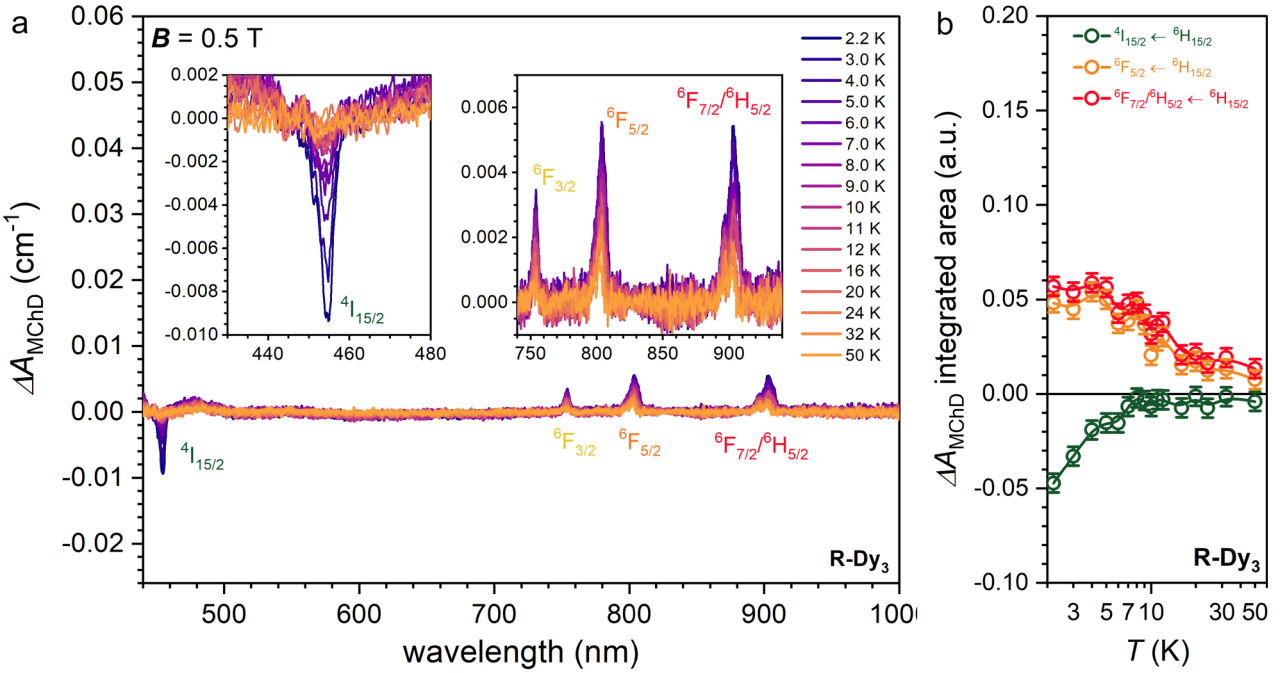

Supplementary Figure 51 (a) Variable-temperature MChD spectra for **R-Dy$_3$** at ***B*** = 0.5 T (***k***,***B*** || (111)). (b) Temperature dependence of the *f-f* electronic transitions with the highest ΔA_{MChD} values. Error bars correspond to twice the uncertainty in the determination of the integrated area of the signals.

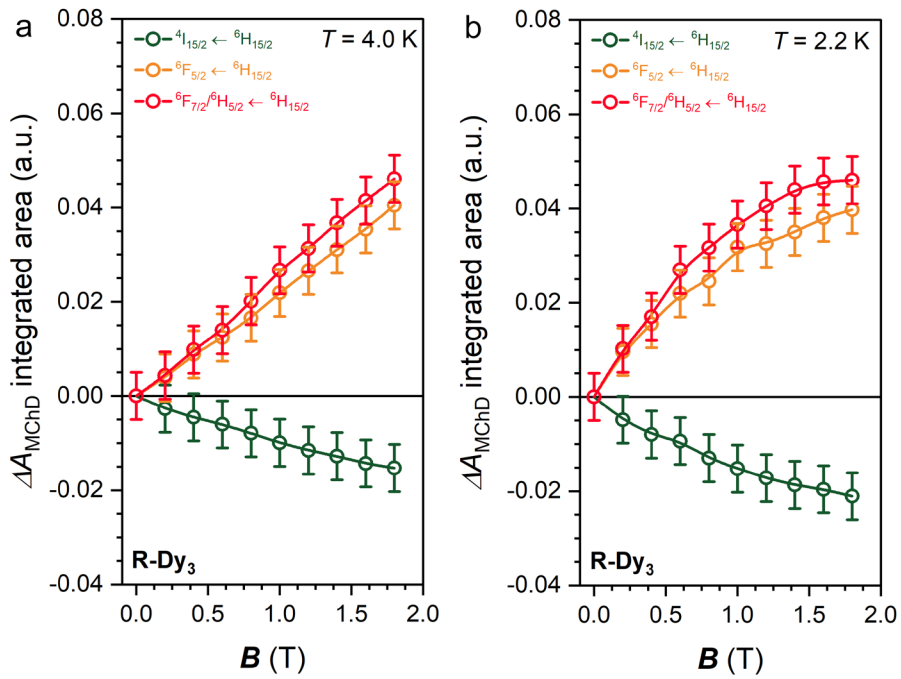

Supplementary Figure 52 Magnetic field dependence for selected *f*-*f* transitions (see legend) at T = 4.0 K (a) and 2.2 K (b) for **R-Dy3** (***k***,***B*** || (111)). Error bars correspond to twice the uncertainty in the determination of the integrated area of the signals.

6. References

1. Hu K.-Q. *et al.* Nickel Ion Induced Multistage Assembly of Th_{13} Cluster. *Nat. Commun.*, **16**, 4000 (2025).
2. Sheldrick G. M. *SHELXT* - integrated space-group and crystal-structure determination. *Acta. Crystallogr. A Found. Adv.*, **71**, 3-8 (2015).
3. Sheldrick G. M. Crystal structure refinement with *SHELXL*. *Acta. Crystallogr. C Struct. Chem.*, **71**, 3-8 (2015).
4. Dolomanov O. V., Bourhis L. J., Gildea R. J., Howard J. A. K., Puschmann H. *OLEX2*: a complete structure solution, refinement and analysis program. *J. Appl. Crystallogr.*, **42**, 339-341 (2009).
5. Ungur L., Chibotaru L. F. Strategies toward High-Temperature Lanthanide-Based Single-Molecule Magnets. *Inorg. Chem.*, **55**, 10043-10056 (2016).
6. Roos B. O., Malmqvist P.-Å. Relativistic quantum chemistry: the multiconfigurational approach. *Phys. Chem. Chem. Phys.*, **6**, 2919-2927 (2004).
7. Szépfalusy P., Kondor I. On the dynamics of continuous phase transitions. *Ann. Phys.*, **82**, 1-53 (1974).
8. Gerry C. C. Coherent states and the Kepler-Coulomb problem. *Phys. Rev. A*, **33**, 6-11 (1986).
9. Roos B. O., Veryazov V., Widmark P.-O. Relativistic atomic natural orbital type basis sets for the alkaline and alkaline-earth atoms applied to the ground-state potentials for the corresponding dimers. *Theor. Chem. Acc.*, **111**, 345-351 (2004).
10. Roos B. O., Lindh R., Malmqvist P.-Å., Veryazov V., Widmark P.-O. New Relativistic ANO Basis Sets for Transition Metal Atoms. *J. Phys. Chem. A*, **109**, 6575-6579 (2005).
11. Roos B. O., Lindh R., Malmqvist P.-Å., Veryazov V., Widmark P.-O., Borin A. C. New Relativistic Atomic Natural Orbital Basis Sets for Lanthanide Atoms with Applications to the Ce Diatom and LuF_3. *J. Phys. Chem. A*, **112**, 11431-11435 (2008).
12. Aquilante F., Gagliardi L., Pedersen T. B., Lindh R. Atomic Cholesky decompositions: A route to unbiased auxiliary basis sets for density fitting approximation with tunable accuracy and efficiency. *J. Chem. Phys.*, **130**, (2009).
13. Pedersen T. B., Aquilante F., Lindh R. Density fitting with auxiliary basis sets from Cholesky decompositions. *Theor. Chem. Acc.*, **124**, 1-10 (2009).
14. Malmqvist P. Å., Roos B. O., Schimmelpfennig B. The restricted active space (RAS) state interaction approach with spin–orbit coupling. *Chem. Phys. Lett.*, **357**, 230-240 (2002).
15. Heß B. A., Marian C. M., Wahlgren U., Gropen O. A mean-field spin-orbit method applicable to correlated wavefunctions. *Chem. Phys. Lett.*, **251**, 365-371 (1996).
16. Malmqvist P. Å., Pierloot K., Shahi A. R. M., Cramer C. J., Gagliardi L. The restricted active space followed by second-order perturbation theory method: Theory and application to the study of CuO_2 and Cu_2O_2 systems. *J. Chem. Phys.*, **128**, (2008).
17. Aquilante F. *et al.* Modern quantum chemistry with [Open]Molcas. *J. Chem. Phys.*, **152**, 214117 (2020).
18. Granovsky A. A. Extended multi-configuration quasi-degenerate perturbation theory: The new approach to multi-state multi-reference perturbation theory. *J. Chem. Phys.*, **134**, 214113 (2011).

19. Chibotaru L. F., Ungur L. Ab initio calculation of anisotropic magnetic properties of complexes. I. Unique definition of pseudospin Hamiltonians and their derivation. *J. Chem. Phys.*, **137**, 064112 (2012).
20. Fdez. Galván I. *et al.* OpenMolcas: From Source Code to Insight. *J. Chem. Theory Comput.*, **15**, 5925-5964 (2019).
21. Ungur L., Chibotaru L. F. Ab Initio Crystal Field for Lanthanides. *Chem. Eur. J.*, **23**, 3708-3718 (2017).
22. Lines M. E. Orbital Angular Momentum in the Theory of Paramagnetic Clusters. *J. Chem. Phys.*, **55**, 2977-2984 (1971).
23. Chibotaru L. F., Ungur L., Soncini A. The Origin of Nonmagnetic Kramers Doublets in the Ground State of Dysprosium Triangles: Evidence for a Toroidal Magnetic Moment. *Angew. Chem., Int. Ed.*, **47**, 4126-4129 (2008).
24. Ungur L., Van den Heuvel W., Chibotaru L. F. Ab initio investigation of the non-collinear magnetic structure and the lowest magnetic excitations in dysprosium triangles. *New J. Chem.*, **33**, 1224-1230 (2009).
25. Li Manni G. *et al.* The OpenMolcas Web: A Community-Driven Approach to Advancing Computational Chemistry. *J. Chem. Theory Comput.*, **19**, 6933-6991 (2023).
26. Noodleman L. Valence bond description of antiferromagnetic coupling in transition metal dimers. *J. Chem. Phys.*, **74**, 5737-5743 (1981).
27. Noodleman L., Case D. A., Aizman A. Broken symmetry analysis of spin coupling in iron-sulfur clusters. *J. Am. Chem. Soc.*, **110**, 1001-1005 (1988).
28. Shoji M. *et al.* A general algorithm for calculation of Heisenberg exchange integrals J in multispin systems. *Chem. Phys. Lett.*, **432**, 343-347 (2006).
29. Neese F. Software update: The ORCA program system—Version 5.0. *WIREs Comput. Mol. Sci.*, **12**, e1606 (2022).
30. Neese F. A perspective on the future of quantum chemical software: the example of the ORCA program package. *Faraday Discuss.*, **254**, 295-314 (2024).
31. Neese F. Software Update: The ORCA Program System—Version 6.0. *WIREs Comput. Mol. Sci.*, **15**, e70019 (2025).
32. Becke A. D. A new mixing of Hartree‐Fock and local density‐functional theories. *J. Chem. Phys.*, **98**, 1372-1377 (1993).
33. Perdew J. P., Ernzerhof M., Burke K. Rationale for mixing exact exchange with density functional approximations. *J. Chem. Phys.*, **105**, 9982-9985 (1996).
34. Pollak P., Weigend F. Segmented Contracted Error-Consistent Basis Sets of Double- and Triple-ζ Valence Quality for One- and Two-Component Relativistic All-Electron Calculations. *J. Chem. Theory Comput.*, **13**, 3696-3705 (2017).
35. Stoychev G. L., Auer A. A., Neese F. Automatic Generation of Auxiliary Basis Sets. *J. Chem. Theory Comput.*, **13**, 554-562 (2017).
36. Neese F. Approximate second-order SCF convergence for spin unrestricted wavefunctions. *Chem. Phys. Lett.*, **325**, 93-98 (2000).